Radiogenic heat production drives Cambrian–Ordovician metamorphism of the Curnamona Province, south-central Australia: Insights from petrochronology and thermal modelling

Alexander T. De Vries Van Leeuwen [a,c,d,*], Tom Raimondo [a,c], Laura J. Morrissey [a,b,c], Martin Hand [c,d], Derrick Hasterok [c], Chris Clark [e], Robert Anczkiewicz [f]

[a] *UniSA STEM, University of South Australia, GPO Box 2471, Adelaide, SA 5001, Australia*

[b] *Mineral Exploration Cooperative Research Centre, Future Industries Institute, University of South Australia, GPO Box 2471, Adelaide, SA 5001, Australia*

[c] *Department of Earth Science, University of Adelaide, Adelaide, SA 5005, Australia*

[d] *Mineral Exploration Cooperative Research Centre, University of Adelaide, Adelaide, SA 5005, Australia*

[e] *The Institute for Geoscience Research (TIGeR), School of Earth and Planetary Sciences, Curtin University, Perth, Australia*

[f] *Kraków Research Centre, Institute of Geological Sciences, Polish Academy of Sciences, Kraków, Poland*

ARTICLE INFO

ABSTRACT

Multi-mineral petrochronology can effectively track changes in the thermochemical environment experienced by rocks during metamorphism. We demonstrate this concept using garnet–chlorite schists from the Walter-Outalpa Shear Zone of the southern Curnamona Province, South Australia, which reveal a cryptic and protracted (c. 39 Myr) record of high thermal gradient metamorphism. Petrochronological data including in situ monazite U–Pb and garnet Lu–Hf and Sm–Nd dating suggest elevated geotherms were persistent between at least c. 519–480 Ma, throughout the duration of garnet growth. Additional in situ xenotime U–Pb dating implies that partial garnet breakdown occurred between c. 480–440 Ma, likely induced by fluid-rock interaction or exhumation. Although metamorphism temporally overlaps with the timing of the regional Delamerian Orogeny (c. 520–480 Ma), the thermal mechanism to sustain elevated temperatures has remained enigmatic. One-dimensional thermal models are used to appraise the role of radiogenic heat production in driving the observed high thermal gradient metamorphism. The models reveal that with only modest crustal thickening during orogenesis, the endogenous radiogenic heat production hosted within the basement rocks could plausibly provide the thermal impetus for metamorphism.

1. Introduction

Different geochronometers often have varying responses to changes in the thermochemical environment during metamorphism (e.g., Kohn et al., 2019; Pyle and Spear, 1999; Rubatto, 2002). The integration of multiple geochronometers from single rock samples with petrological information can therefore provide valuable insights into the timing, duration and thermal character of metamorphism (e.g., Kohn et al., 2019). This approach is particularly valuable in terranes that have complex or cryptically preserved metamorphic histories. Shear zones are prime candidates for this type of investigation because they often record multiple phases of reactivation or overprinting metamorphic events that are not overtly recorded elsewhere in the terrane (e.g., Mahan et al., 2006; Prent et al., 2020).

The southern Curnamona Province of south-central Australia (Fig. 1) has a complex polymetamorphic history. The Palaeo- to Mesoproterozoic basement rocks of the Willyama Supergroup (Fig. 1b) underwent regional metamorphism at upper greenschist- to granulite-facies during the c. 1600–1580 Ma Olarian Orogeny (e.g., Clarke et al., 1986; De Vries Van Leeuwen et al., 2022; Forbes et al., 2008). This is the most widespread and commonly represented metamorphic signature of the terrane. Subsequent metamorphism occurred at greenschist- to amphibolite-facies conditions during the c. 520–480 Ma Delamerian Orogeny (e.g., Clark and Hand, 2010; Dutch et al., 2005; Foden et al., 2006). This episode of metamorphism is sporadically recorded in the Willyama Supergroup, the overlying Neoproterozoic to Early Cambrian

---

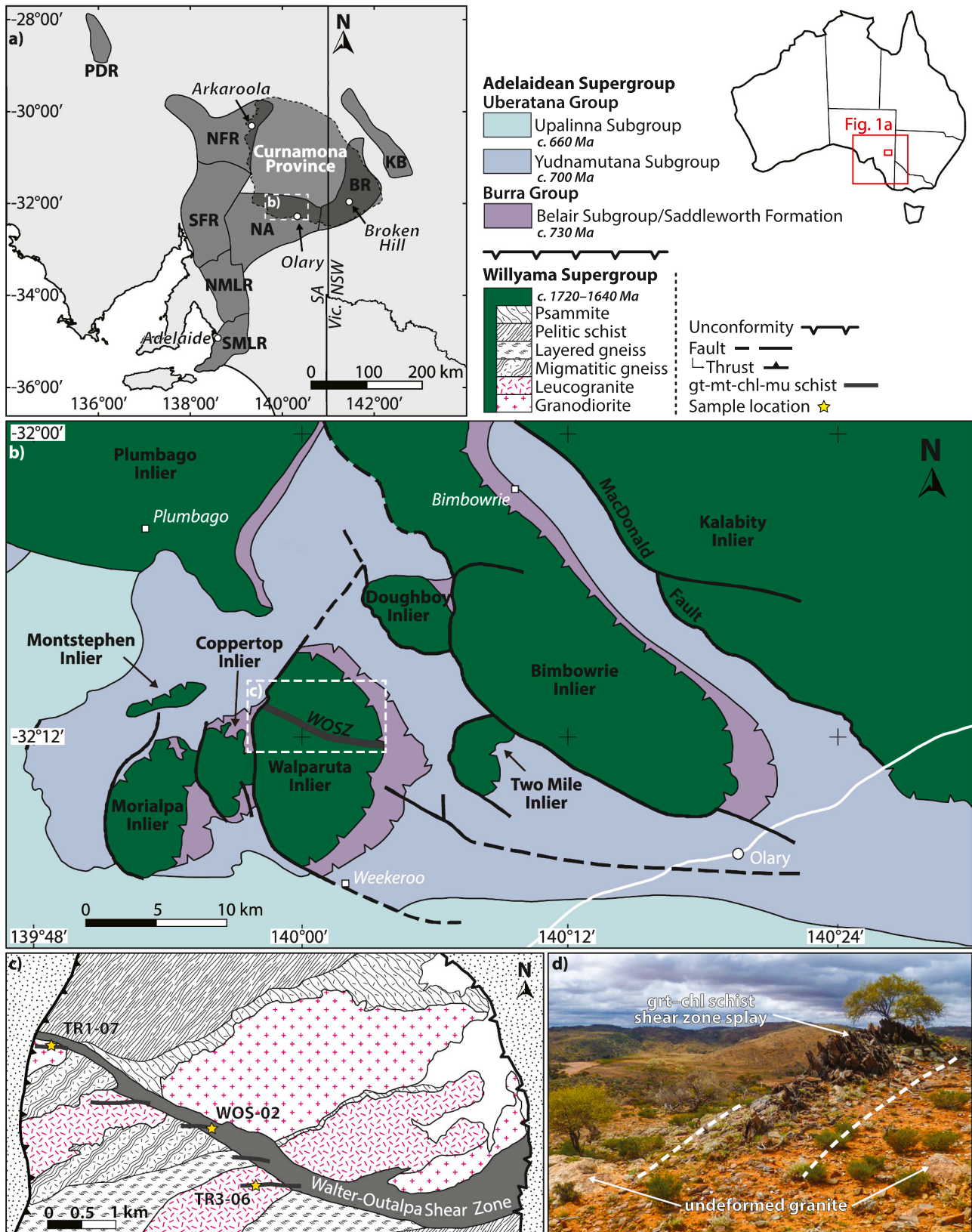* Corresponding author at: Department of Earth Science, University of Adelaide, Adelaide, SA 5005, Australia.
  E-mail address: alexander.devriesvanleeuwen@adelaide.edu.au (A.T. De Vries Van Leeuwen).

Fig. 1. (a) Generalised location map of the Curnamona Province and Adelaide Superbasin; (b) Simplified geological map of the Willyama Inliers in southern Curnamona Province; (c) Detailed geological map of the central Walparuta Inlier detailing where samples were collected from the Walter-Outalpa Shear Zone. Ages of the Adelaidean Supergroup lithologies are from the interpolated stratigraphic ages of Preiss (2000), and the age of the Willyama Supergroup is summarised in Conor and Preiss (2008); (d) Field photo (facing NE) depicting the garnet–chlorite shear zone splay where sample TR1-07 was collected. For further information about field-scale features, see Clark et al. (2006). Abbreviations in panel (a) are as follows: **PDR** = Peake and Denison Ranges; **KB** = Koonenbery Belt; **BR** = Barrier Ranges; **NA** = Nackara Arc; **NFR** = Northern Flinders Ranges; **SFR** = Southern Flinders Ranges; **NMLR** = Northern Mount Lofty Ranges; **SMLR** = Southern Mount Lofty Ranges.

(meta)sedimentary successions of the Adelaide Superbasin (e.g., Clark and Hand, 2010; Rutherford et al., 2006), and in reactivated shear zones that dissect the terrane (Fig. 1; Clark et al., 2006; Dutch et al., 2005).

During the Delamerian Orogeny, the Curnamona Province resided inboard of the active palaeo-Pacific continental margin of Gondwana (Foden et al., 2006; Glen, 2013; Greenfield et al., 2011; Johnson et al., 2016). Various models exist to explain the geodynamic setting at this time, with most favouring west-dipping subduction (present-day co-ordinates) as the main driver for crustal thickening (e.g., Foden et al., 2006; Glen, 2013; Greenfield et al., 2011). Many of these models also suggest that subduction was punctuated by periods of slab rollback and trench retreat (Collins, 2002; Johnson et al., 2016). Such environments can generate high thermal gradients in backarc regions via increased mantle heat flow associated with asthenospheric upwelling and concomitant magmatism (e.g., Collins, 2002; Hyndman et al., 2005). In the Adelaide Superbasin, much of the high-grade metamorphism is spatially and temporally associated with Delamerian-aged magmatic rocks (Dymoke and Sandiford, 1992; Foden et al., 2006), in line with metamorphism occurring in a backarc environment. However, there is a dearth of Delamerian-aged magmatic rocks that intrude the Willyama Supergroup, suggesting a separate mechanism may have been responsible for driving metamorphism in the Curnamona Province.

Delamerian deformation was largely partitioned into the flanking successions of the Adelaide Superbasin (Fig. 1; e.g., Lloyd et al., 2020; Paul et al., 1999; Paul et al., 2000), with the older basement rocks of the Willyama Supergroup acting as a rigid block. However, in parts of the southern and northwestern Curnamona Province, these basement rocks were reactivated along discrete shear zones (Paul et al., 1999; Paul et al., 2000). This contrasting thick- and thin-skinned deformational style during the Delamerian Orogeny has been correlated to changes in sedimentary thickness and heat flow, where more deeply buried crust is typically hotter and rheologically weaker, thus able to facilitate deformation of the basement (Paul et al., 1999; Paul et al., 2000; Sandiford et al., 1998b). In the southern Curnamona Province, several studies have highlighted the presence of elevated levels of heat producing elements (K, Th, and U) in the basement lithologies, leading to high radiogenic heat production (Alessio et al., 2018; De Vries Van Leeuwen et al., 2021; De Vries Van Leeuwen et al., 2022; McLaren et al., 2006; Neumann et al., 2000). Whereas the mechanism(s) behind the generation of such high heat-producing crust can be wide-ranging (e.g., Korhonen and Johnson, 2015; McLaren and Powell, 2014), it is clear that elevated levels of radiogenic heat produced in the mid- to upper-crust represent a potential driver for the high thermal gradient metamorphism experienced during the Delamerian Orogeny, and its persistence over ~40 Myr (Sandiford et al., 1998a; Sandiford et al., 1998b). As such, assessing the role of radiogenic heating in the southern Curnamona Province during the Delamerian Orogeny is key to understanding its thermal evolution.

This study investigates garnet–chlorite schists from splays of the Walter-Outalpa Shear Zone (WOSZ; Fig. 1). The WOSZ forms one of a series of broadly east–west-trending shear zones that dissect the southern Curnamona Province and record Delamerian ages. Previous dating of the WOSZ splays using various techniques and geochronometers yield a spread of dates between 531 and 491 Ma (Clark et al., 2006; Dutch et al., 2005; Raimondo et al., 2013). These data suggest that shear zones in the southern Curnamona Province remained active throughout the Delamerian Orogeny for a period of at least c. 40 Myr. However, many of these dates were obtained using garnet Lu–Hf or Sm–Nd geochronology, relying on assumptions about the growth behaviour of garnet during metamorphism (e.g., Kohn, 2009), or via U–Pb monazite dating using EPMA, which has proven to be problematic when dealing with discordant data (e.g., Suzuki and Kato, 2008). Furthermore, the existing geochronological data have been derived from shear zone samples with disparate compositions and mineral assemblages, further complicating direct comparison. With these details in mind, it is clear that unravelling the thermochemical evolution of the shear zones and appraising their apparent c. 40 Myr evolution is not feasible using existing data alone.

As such, we attempt to construct a coherent model for the evolution of the WOSZ with a new approach. This is done via the collection of in situ LA–ICP–MS monazite and xenotime U–Pb geochronological and geochemical data, together with MC–ICP–MS garnet Lu–Hf and Sm–Nd geochronological data and LA–ICP–MS trace element maps, from a suite of garnet–chlorite schists. These data are integrated to construct a revised petrochronological framework for the WOSZ, then combined with one-dimensional thermal modelling to evaluate the role of radiogenic heating in driving high thermal gradient metamorphism during the Delamerian Orogeny.

2. Geological background

2.1. Regional stratigraphy and metamorphic framework

The southern Curnamona Province is comprised of a sequence of Palaeoproterozoic basement rocks known as the Willyama Supergroup (Fig. 1). This succession is dominated by clastic metasedimentary rocks, ranging from pelitic to psammitic compositions with subordinate volcanic, volcaniclastic, and intrusive lithologies, considered to have been deposited between c. 1720–1640 Ma in an epicontinental rift basin (e.g., Conor and Preiss, 2008; Page et al., 2005). At present, the Willyama Supergroup is exposed in a series of basement inliers in eastern South Australia and western New South Wales (Fig. 1). On the basis of the metamorphic grade attained during the c. 1600–1580 Olarian Orogeny, the Willyama Supergroup in the southern Curnamona Province is divided into two domains, with the Olary Block in the southwest hosting lower grade greenschist- to amphibolite-facies rocks whilst the Broken Hill Block in the southeast is dominated by upper-amphibolite- to granulite-facies rocks (e.g., Webb and Crooks, 2003).

Overlying the Willyama Supergroup is a sequence of Neoproterozoic to mid-Cambrian sedimentary rocks, collectively referred to as the Adelaidean Supergroup (Fig. 1), which were deposited between c. 840–500 Ma (e.g., Lloyd et al., 2020; Preiss, 2000). The Adelaidean Supergroup is comprised of clastic sedimentary rocks ranging from shales to sandstones with lesser carbonate and volcanic/volcaniclastic units deposited into a long-lived rift basin (the Adelaide Superbasin), with late-stage deposition being largely accommodated via thermal subsidence (e.g., Lloyd et al., 2020; Preiss, 2000). Between c. 520–480 Ma, both the Willyama and Adelaidean supergroups were variably overprinted by a second phase of high thermal gradient metamorphism associated with the Delamerian Orogeny (e.g., Clark et al., 2006; Clark and Hand, 2010; Clarke et al., 1987; Dutch et al., 2005; Rutherford et al., 2006). During the Delamerian Orogeny, the Curnamona Province is thought to have acted as a rigid block, around which deformation was largely accommodated via thin-skinned inversion and oroclinal bending of the Adelaide Superbasin (Fig. 1; Musgrave, 2015; Paul et al., 1999; Paul et al., 2000). However, along the southern and northwestern margins of the Curnamona Province deformation was thick-skinned, involving exhumation of the underlying basement rocks belonging to the Willyama Supergroup (Paul et al., 1999; Paul et al., 2000). This transition from thin- to thick-skinned deformation has been linked with observed increases in the thickness of the overlying Adelaidean succession, with deformation largely being associated with reactivation of existing crustal shear zones (Paul et al., 1999; Paul et al., 2000; Sandiford et al., 1998b).

In the southern Curnamona Province, metamorphism during the Delamerian Orogeny occurred under high-temperature–low-pressure (HT–LP) conditions, characterised by apparent thermal gradients ranging from ~30–40 °C km^{-1} (e.g., Clark et al., 2006; Clark and Hand, 2010; Dutch et al., 2005). Its regional expression is more pervasive in the Olary Block, where Delamerian mineral assemblages are frequently observed overprinting existing Olarian assemblages (Clark and Hand, 2010; Rutherford et al., 2006). In the Broken Hill Block its expression is largely limited to shear zones that dissect the Willyama Supergroup (e. g., Clark et al., 2006; Dutch et al., 2005; Raimondo et al., 2013;

Rutherford et al., 2006). These shear zones are thought to have initially formed during the late stages of the Olarian Orogeny (Clark et al., 2006; Clarke et al., 1986; Clarke et al., 1987; Dutch et al., 2005), and were reactivated and rehydrated as extensional faults during the opening of the Adelaide Superbasin at c. 840 Ma (e.g.,Clark et al., 2006; Raimondo et al., 2013). Following deposition of the 10–12 km thick Adelaidean Supergroup between c. 840–500 Ma (e.g., Dutch et al., 2005; Lloyd et al., 2020; Preiss, 2000), thick-skinned deformation of the Adelaidean and Willyama Supergroups during Delamerian compression (e.g., Paul et al., 1999; Paul et al., 2000) buried these now hydrous fault rocks to mid-crustal depths, sufficient to generate the amphibolite-facies mineral assemblages frequently observed in the shear zones (Clark et al., 2006; Dutch et al., 2005; Raimondo et al., 2013).

2.2. Walter-Outalpa Shear Zone

The Walter-Outalpa Shear Zone is perhaps the prime example of a reactivated and polymetamorphic shear zone in the Curnamona Province. It is hosted in the Walparuta Inlier, a basement inlier exposing rocks of the Willyama Supergroup in the Olary Block (Fig. 1). At its eastern margin, the WOSZ is unconformably overlain by sedimentary rocks of the Adelaidean Supergroup (Fig. 1c), indicating a prior phase of deformation attributed to the c. 1600–1580 Ma Olarian Orogeny (Clarke et al., 1986). In contrast, at its western margin it displaces and overprints Adelaidean sedimentary sequences, and records widespread evidence of structural reactivation and metasomatism during the c. 520–480 Ma Delamerian Orogeny (Clark et al., 2006; Dutch et al., 2005; Raimondo et al., 2013).

The WOSZ dissects Palaeoproterozoic to Mesoproterozoic granitoids of the c. 1710 Basso Suite and the c. 1580 Ma Ninnerie Supersuite (Ashley et al., 1996; Page et al., 2005; Wade, 2011), along with Late Palaeoproterozoic metasedimentary rocks of the c. 1720–1640 Ma Willyama Supergroup (Conor and Preiss, 2008), forming an east–west trending interconnected network of schists and mylonites that sharply intersect the host lithologies (Fig. 1; Clark et al., 2006; Raimondo et al., 2013). The exposed portion of the WOSZ is approximately 10 km long and varies in width between 100 and 400 m (Fig. 1). In zones where the WOSZ intersects Palaeoproterozoic to Mesoproterozoic granitoids, narrow splays from the main shear zone are observed that vary in width between 2 and 10 m and host garnet–chlorite schists (Fig. 1d; Clark et al., 2006; Raimondo et al., 2013). Whole rock and garnet oxygen isotope data from these assemblages demonstrate that during reactivation associated with c. 840 Ma rifting, fault rocks of the WOSZ were hydrated via interaction with meteoric fluids in the near-surface environment (Clark et al., 2006; Raimondo et al., 2013), followed by burial under the Adelaidean Supergroup successions.

Phase equilibria modelling of metapelite hosted in the WOSZ suggests peak metamorphic conditions reached 534 ± 20 °C at 5.0 ± 0.8 kbar (Dutch et al., 2005), corresponding to apparent thermal gradients between 95 and 123 °C kbar^{-1} (~32–41 °C km^{-1}). These results are supported by garnet–chlorite thermometry from the same garnet–chlorite shear zone splays analysed in this study, yielding a mean temperature of 526 ± 13 °C (Clark et al., 2006). Pressures of c. 5 kbar were plausibly generated via the inferred 10–12 km thickness of the overlying Adelaidean Supergroup coupled with 10–20% crustal thickening associated with the Delamerian Orogeny (Paul et al., 1999; Preiss, 2000). EPMA monazite U–Pb geochronology from these metapelitic and garnet–chlorite schists yield dates between 506 and 491 Ma (Clark et al., 2006; Dutch et al., 2005), whereas garnet hosted in the garnet–chlorite schists yield Lu–Hf dates between 531 and 515 Ma (Raimondo et al., 2013). These data indicate that the shear zone records a prolonged metamorphic history, perhaps pre-dating the main phase of the Delamerian Orogeny (e.g., Foden et al., 2006), although the precise correspondence between its temporal and metamorphic evolution is unresolved.

2.3. Heat production and drivers for metamorphism

Throughout the southern Adelaide Superbasin and Koonenbery Belt (Fig. 1), advective heating via granitic magmatism has been proposed as the main driver for localised high thermal gradient metamorphism during the Delamerian Orogeny (e.g., Foden et al., 2006; Foden et al., 2020; Greenfield et al., 2011; Johnson et al., 2016; Sandiford et al., 1992; Sandiford et al., 1995). However, there is no significant magmatism associated with the Delamerian Orogeny in the Curnamona Province, with a dearth of Delamerian-aged magmatic rocks having intruded the Willyama Supergroup (e.g., Foden et al., 2020; Johnson et al., 2016), bringing in to question the thermal driver for metamorphism in the region.

An alternate hypothesis is that heating was driven by radiogenic heat production. Rocks of the Willyama Supergroup have anomalous enrichments in heat producing elements (K, Th, and U) and hence elevated levels of radiogenic heat production (De Vries Van Leeuwen et al., 2022; McLaren et al., 2006; Neumann et al., 2000). Alessio et al. (2018) reports mean heat production values from sub- and suprasolidus metasedimentary rocks of the Willyama Supergroup to be 2.65 and 3.30 μW m^{-3}, respectively. These values are much higher than values of typical metasedimentary rocks (~1–2 μW m-3; see Hasterok et al., 2018). Additionally, when compared to the global median value for granitic rocks of 2.7 μW m^{-3} (Hasterok et al., 2018), granitoids belonging to the Ninnerie Supersuite that intrude the Willyama succession in the study area (Wade, 2011) yield significantly higher heat production values of 3.2–4.6 μW m^{-3} (see Fig. 17 in De Vries Van Leeuwen et al., 2022), boosting the total heat production of the basement. Such enhanced radiogenic heat production corresponds to anomalously high heat flow, with measured values from the central and southern Curnamona Province ranging between 79 and 103 mW m^{-2} (Jones et al., 2011). This regional trend continues into the eastern Gawler Craton where correlative basement rocks (e.g., Giles et al., 2004) also exhibit high radiogenic heat production, forming a broad province known as the South Australian Heat Flow Anomaly (SAHFA; see Neumann et al., 2000).

3. Sample descriptions and petrography

Garnet–chlorite schists from the WOSZ analysed in this study were collected from the eastern (TR3-06), central (WOS-02), and western (TR1-07) shear zone splays (Fig. 1c), and have previously been characterised by Clark et al. (2006) and Raimondo et al. (2013). The samples comprise the mineral assemblage garnet–chlorite–magnetite–muscovite–quartz. Garnet porphyroblasts are up to 1 cm in diameter and are wrapped by a strong shear fabric defined by elongated chlorite and muscovite. In samples TR1-07 and TR3-06, the fabric can be further differentiated into chlorite-rich and muscovite-rich domains (Fig. 2a). Coarse-grained chlorite and muscovite also commonly occur in the pressure shadows of garnet (Fig. 2b) as well as overprinting the shear fabric at high angles (Fig. 2c). Rare domains of granoblastic quartz occur in the matrix and in garnet pressure shadows (Fig. 2a,b). Magnetite is up to 5 mm long in sample WOS-02 and typically ranges between 0.1 and 1 mm in TR1-07 and TR3-06. It occurs both as inclusions within garnet and as porphyroblasts that overprint the chlorite–muscovite fabric (Fig. 2a,c), and is most abundant in the chlorite-rich domains of TR1-07 and TR3-06 (Fig. 2a). Garnet is variably replaced by chlorite along fractures and grain boundaries, in some instances exhibiting near-total replacement (Fig. 2b,d), whereas in other instances it shows no evidence of chlorite replacement (Fig. 2e). Minor goethite occurs at the margins of garnet and matrix minerals and partially replaces magnetite in sample WOS-02 (Fig. 2f). Accessory monazite, xenotime and zircon (likely inherited) are present throughout each sample in varying abundances. Zircon is hosted as inclusions within garnet and throughout the matrix. Petrographic descriptions of monazite and xenotime are provided in the Results section below.
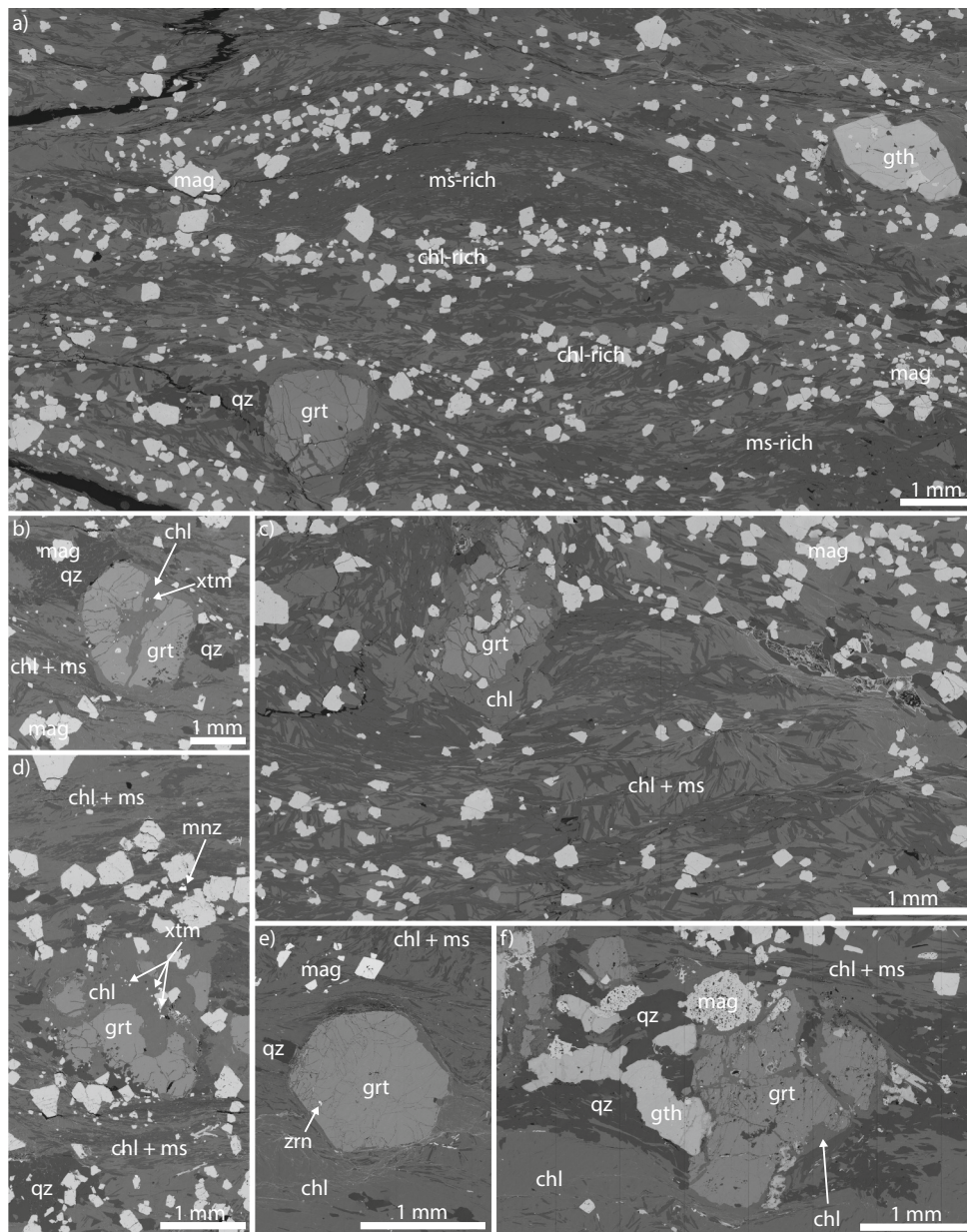
Fig. 2. Back-scattered electron images of garnet–chlorite schist samples. (a) Alternating chlorite- and muscovite-rich domains in sample TR3-06, with magnetite occurring in higher abundance in chlorite-rich domains; (b) Coarse muscovite, chlorite and quartz occurring in the pressure shadows of a garnet porphyroblast partially replaced by chlorite in sample TR1-07. Note the presence of xenotime hosted in chlorite that replaces garnet; (c) Chlorite and muscovite laths at high angles to the shear fabric in sample TR3-07. Garnet is partially replaced by chlorite and hosts numerous inclusions of magnetite; (d) Garnet in sample TR1-07 with near complete replacement by chlorite, which itself hosts numerous inclusions of xenotime; (e) Euhedral garnet porphyroblast in sample WOS-02; (f) Goethite partially replacing magnetite in sample WOS-02. Garnet also exhibits partial breakdown to chlorite, in contrast with the euhedral, unaltered garnet from the same sample pictured in (e). Mineral abbreviations after Whitney and Evans (2010).

4. Methods

Detailed methods for garnet compositional mapping, garnet geochronology, and accessory mineral U–Pb geochronology and REE geochemistry are available in Appendix A. Selected garnet compositional maps for major elements are presented in Fig. 3 and trace element maps and traverses pertinent to the interpretation of the Lu–Hf and Sm–Nd garnet geochronology are shown in Figs. 4 and 5. All garnet compositional maps are provided in Appendix B. Garnet geochronology results are presented in Fig. 6 and the data are available in Tables 1 and 2. Garnet Lu–Hf geochronology is originally published in Raimondo et al. (2013) and is presented here for direct comparison with new Sm–Nd data. Monazite backscattered electron (BSE) images are presented in Fig. 7, concordia plots in Fig. 8, and REE spiderplots in Fig. 9. Xenotime BSE images are presented in Fig. 10, concordia plots in Fig. 11, and REE spiderplots in Fig. 12. All monazite and xenotime U–Pb geochronological and REE geochemical data are provided in Appendices C and D, respectively.

5. Results

5.1. Garnet major and trace element zoning

Garnet major element maps from all samples reveal zoning patterns consistent with prograde growth zoning (Fig. 3). Mn decreases from ~20 wt% in garnet cores radially outwards to values of ~10 wt% at the rims. Fe and Mg show the inverse of this pattern, increasing from cores to rims. Ca in samples TR1-07 and WOS-02 is comparatively unzoned, whereas sample TR3-06 shows a sharp decrease in Ca concentrations between the core and rim domain (Fig. 3f). Garnet in all samples show marked REE zoning. Generally, core domains exhibit elevated REE in the innermost cores that deplete radially outward, whereas rim domains have comparatively lower REE concentrations (Figs. 4 and 5).

In sample TR1-07, garnet has the highest concentration of Sm and Gd at the innermost core, depleting radially outward towards a minimum at the core-rim boundary before gradually increasing towards the outermost rim (Fig. 4a,b; 5a). Lu is strongly concentrated in the core domain, exhibiting a sharp decline in concentration across the core-rim interface
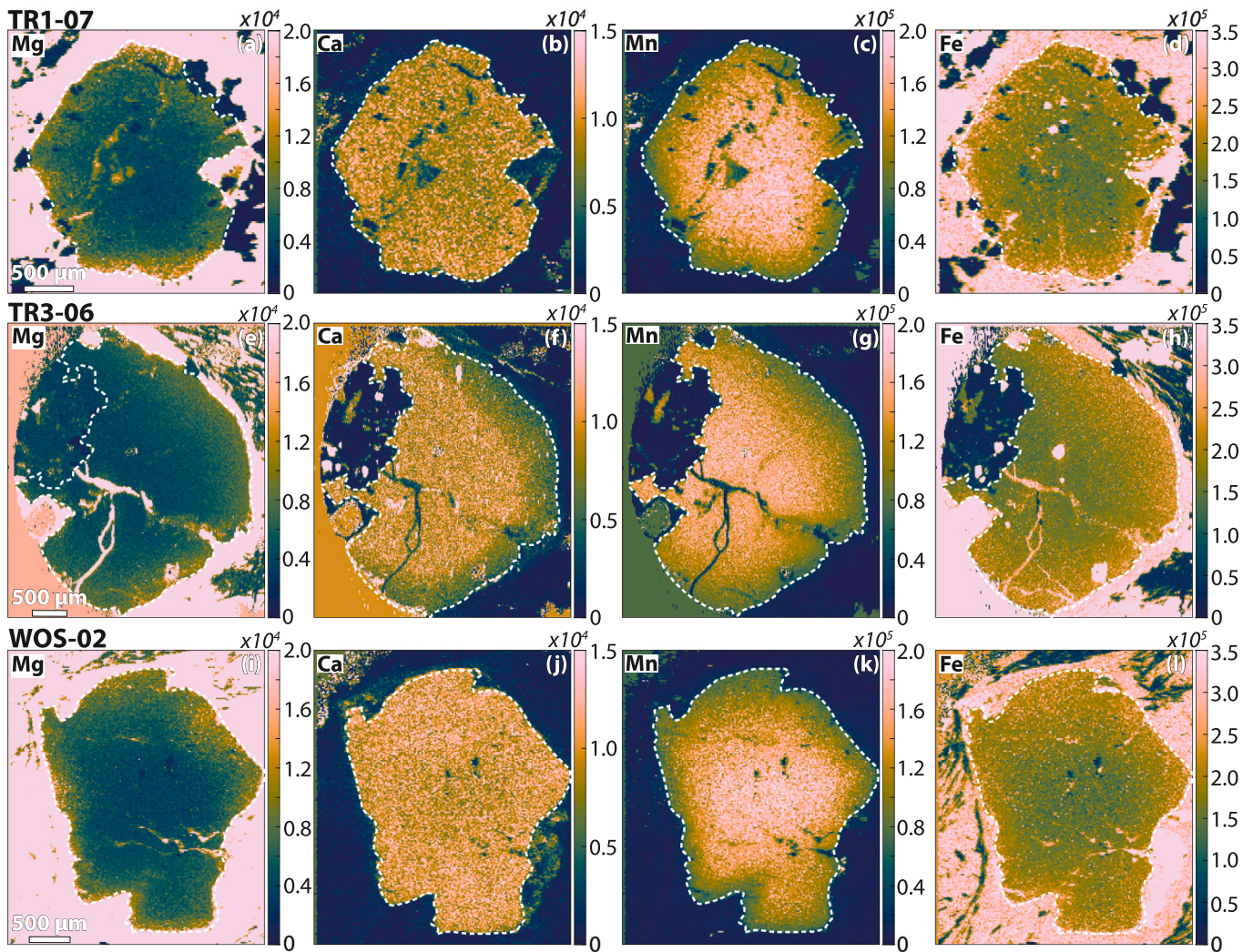
Fig. 3. Garnet major element compositional maps from samples TR1-07 (a–d), TR3-06 (e–h), and WOS-02 (i–l). Maps were generated using XMapTools 3.4 (Lanari et al., 2014).

from ~35 ppm to ~5 ppm (Fig. 4c; 5a). In sample TR3-06, similar trends are seen in Sm and Lu as those outlined for sample TR1-07. However, a much sharper boundary between the core and rim domains can be seen, mimicking the boundary observed in the Ca map (Figs. 3f; 4e,g). For Sm, the core domain has a concentration of ~5 ppm, which sharply drops to ~1.5 ppm across the core-rim boundary with no noticeable increase towards the outermost rim, unlike TR1-07 (Fig. 5b). Additionally, the Lu map shows a distinct annulus where the concentration reaches a local maximum at the core-rim boundary. Sample WOS-02 has a significantly thinner rim (~200 μm) in contrast to the other samples. The core domain has relatively flat Sm zoning, whereas Lu is strongly concentrated in the innermost core, depleting radially outward into Lu-poor rims (Fig. 4; 5c). As in sample TR3-06, the rim is depleted in Sm and Lu in comparison to the core, with no perceivable increase in Sm towards the outermost rim. Notably, Lu-depletion in the rim is much broader than that seen in Sm (~500 μm versus ~200 μm).

Zr maps for each sample are provided to highlight the distribution of zircon along with other phases that are likely to influence the Hf content of garnet if present as inclusions. Zircon inclusions appear as 'hotspots' in both the Lu and Zr maps, with regions highlighted with red pixels in the Zr maps in panels d, h, and l of Fig. 4 corresponding to concentrations higher than 20,000 ppm. Magnetite inclusions within garnet are also elevated in Zr. Fractures with elevated Zr concentrations are dominantly comprised of goethite.

5.2. Garnet Lu–Hf and Sm–Nd geochronology

Lu–Hf and Sm–Nd isochrons were constructed using 3–6 bulk garnet fractions along with a whole-rock fraction. Lu–Hf isochrons yield dates of 518.9 ± 1.5 Ma ($n = 4$, MSWD = 0.31, $p = 0.73$) for sample TR1-07, 515.1 ± 1.0 Ma ($n = 7$, MSWD = 0.31, $p = 0.90$) for sample TR3-06, and 531.4 ± 1.1 Ma ($n = 7$, MSWD = 1.40, $p = 0.23$) for sample WOS-02 (Fig. 6a–c). Sm–Nd data are consistently younger than Lu–Hf, yielding dates of 479.8 ± 1.2 Ma ($n = 4$, MSWD = 1.60, $p = 0.20$) for sample TR1-07, 487.1 ± 3.7 Ma ($n = 4$, MSWD = 0.16, $p = 0.85$) for sample TR3-06, and 501.7 ± 1.1 Ma ($n = 7$, MSWD = 5.00, $p = 0.00$) for sample WOS-02 (Fig. 6d–f). Hf concentrations (Table 1) are significantly higher than typical values of garnet (~100 ppb; Anczkiewicz et al., 2004), whereas Nd concentrations fall within typical ranges (e.g., Anczkiewicz et al., 2004). The observed elevation in Hf may be due to minor zircon contamination, particularly in sample WOS-02, which yields a significantly older Lu–Hf date and has much higher measured Hf concentrations than the other samples.

5.3. Monazite U–Pb geochronology and REE geochemistry

Monazite forms two distinct morphologies. The first variety (mnz$_1$) forms subhedral, typically equant grains of variable size between 50 and 200 μm (Fig. 7a–c,i–k). The relationship between these grains and the
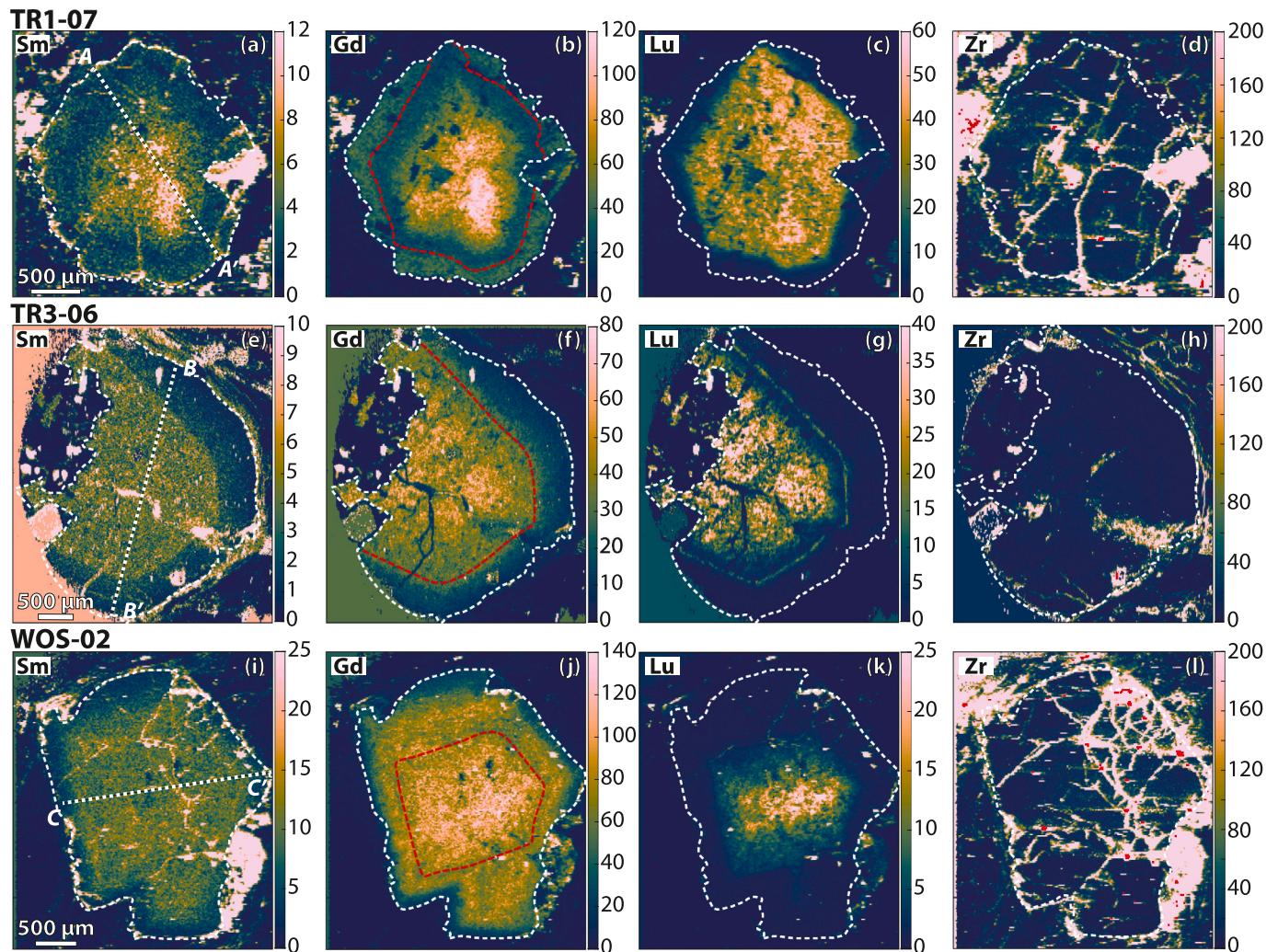
Fig. 4. Garnet trace element compositional maps from samples TR1-07 (a–d), TR3-06 (e–h), and WOS-02 (i–l). Gd maps are presented to better visualise the distribution of Sm, whereas Zr maps are presented as a proxy for Hf and show the distribution of zircon (red pixels) throughout the garnet grains. Dashed white lines labelled A–A', B–B′ and C–C′ indicate the transects shown in Fig. 6. Maps were generated using XMapTools 3.4 (Lanari et al., 2014). Red dashed lines presented on the Gd maps are depict core–rim boundaries. (For interpretation of the references to colour in this figure legend, the reader is referred to the web version of this article.)

chlorite–muscovite fabric is unclear, although they often form as inclusions within minerals aligned with the fabric. The second variety (mnz$_2$) comprises anhedral, inclusion-rich grains of variable size between 50 and 400 μm (Fig. 7d–f,g,h,l) that commonly exhibit embayed grain boundaries and are frequently observed as aggregates of multiple individual grains. Both varieties occur throughout the matrix, with no clear affinity for specific matrix minerals. Rare grains of mnz$_1$ also occur as inclusions within garnet. Back-scattered electron (BSE) images of selected monazite grains show that anhedral, inclusion-rich grains belonging to mnz$_2$ have a homogeneous BSE response, whereas the subhedral, equant grains in mnz$_1$ often exhibit faint patchy zoning (Fig. 7), with rare grains showing concentric zoning (Fig. 7i).

5.3.1. TR1-07

Eighty-one analyses were collected from 63 individual monazite grains in sample TR1-07. From these, 28 were excluded from weighted mean calculations based on discordance (i.e., if the 2SE error ellipse of an analysis does not intercept the concordia curve). Two concordant analyses from matrix-hosted grains yield considerably older ^{206}Pb/^{238}U dates of 538 ± 16 Ma and 531 ± 10 Ma. Monazite belonging to the mnz$_1$ subpopulation yield a spread of concordant ^{206}Pb/^{238}U dates between c. 516 and 474 Ma and include the two older grains (c. 538 and 531 Ma), whereas monazite from the mnz$_2$ subpopulation falls into a tighter range

between c. 502 and 480 Ma (Fig. 8a). Combining all discordant and concordant analyses from the mnz$_2$ subpopulation defines a lower intercept age of 479 ± 8 Ma (n = 39, MSWD = 1.30, p = 0.12; Fig. 8a), whereas concordant analyses from mnz$_2$ yield a weighted mean ^{206}Pb/^{238}U date of 491 ± 2 Ma (n = 24, MSWD = 1.41, p = 0.09; Fig. 8a). Concordant analyses from both mnz$_1$ and mnz$_2$ have consistent REE geochemical characteristics. Y + HREE concentrations are spread between 8981 and 17,594 ppm. HREE slopes fall between Gd$_N$/Yb$_N$ values of 160–765, with analyses from mnz$_1$ having marginally steeper slopes (Fig. 9a). Th/U ratios are also variable, yielding a spread between 0.9 and 60.2. There are no discernible trends between monazite geochemistry and U–Pb age.

5.3.2. TR3-06

Fourteen analyses were collected from 13 individual monazite grains in sample TR3-06. All monazite analysed from this sample are anhedral, inclusion-rich grains, consistent with the mnz$_2$ subpopulation observed in the other samples. All but one of these analyses are discordant. Two analyses have much higher concentrations of ^{204}Pb (11 and 21 ppm) and were excluded. The remaining 12 analyses track along a common Pb trend that defines an imprecise discordia with a lower intercept age of 482 ± 6 Ma (n = 12, MSWD = 3.60, p = 0.00; Fig. 8b) when anchored to an initial common ^{207}Pb/^{206}Pb ratio of 1.106 (Stacey and Kramers,
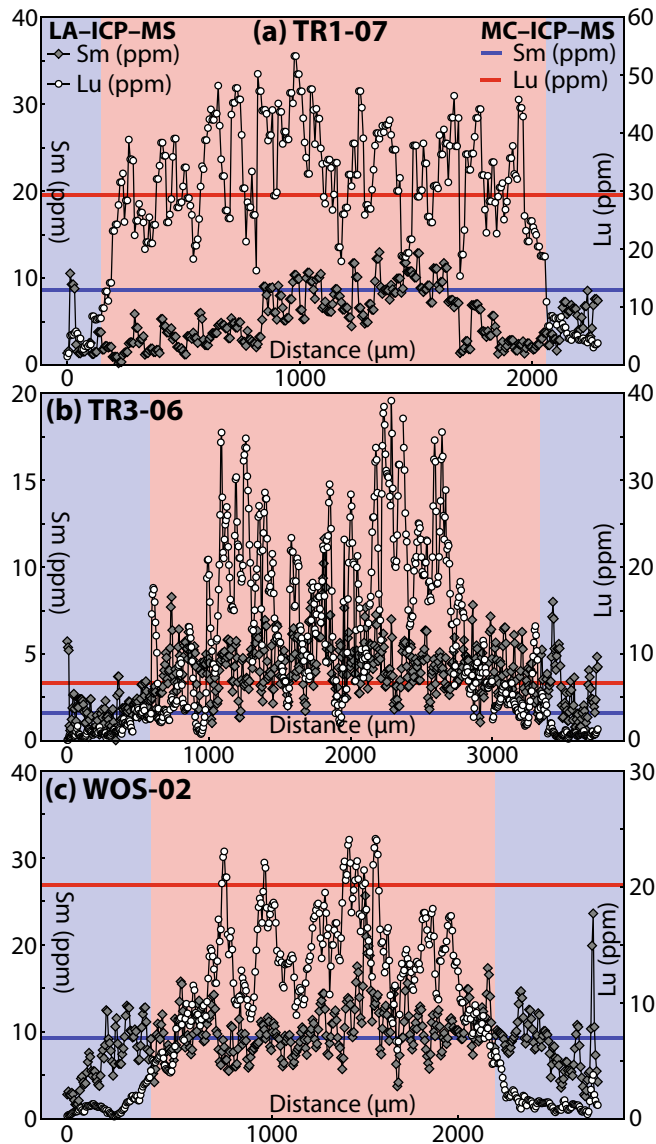
Fig. 5. Garnet core-to-rim compositional traverses for Sm and Lu following the transects (dashed white lines) depicted in Fig. 4. Red and blue shaded areas correspond to core and rim domains, respectively. (For interpretation of the references to colour in this figure legend, the reader is referred to the web version of this article.)

1975). The single concordant analysis yields a ^{206}Pb/^{238}U date of 488 ± 11 Ma, Y + HREE concentration of 19,283 ppm, a Gd_N/Yb_N value of 199, and a Th/U ratio of 41. Discordant analyses that define the discordia used to calculate the lower intercept age all exhibit similar geochemical characteristics (Fig. 9b).

5.3.3. WOS-02

Seventy-nine analyses were collected from 71 individual monazite grains in sample WOS-02. From these, 53 were excluded from weighted mean calculations based on discordance. Concordant monazite from the mnz_1 subpopulation yield ^{206}Pb/^{238}U dates between c. 495 and 472 Ma, whereas two concordant analyses from the mnz_2 subpopulation yielded ^{206}Pb/^{238}U dates of 486 and 485 Ma. Combining all discordant and concordant analyses from the mnz_2 subpopulation, where discordant analyses have ^{204}Pb concentrations <5 ppm, defines a lower intercept age of 480 ± 10 Ma ($n = 10$, MSWD = 1.80, $p = 0.08$; Fig. 8c). There are no clear links between either the morphological style (mnz_1 vs. mnz_2) or BSE zoning patterns and U–Pb age. Concordant analyses from both mnz_1

and mnz_2 have some geochemical variability but do not define separate groups. Y + HREE concentrations are spread between 1454 and 4890 ppm, much lower than the values from samples TR1-07 and TR3-06. HREE slopes are quite variable (Fig. 9c), falling between Gd_N/Yb_N values of 1069–9394. Th/U values are also variable, spread between 0.9 and 36.1. There are no discernible trends between monazite geochemistry and U–Pb age.

5.4. Xenotime U–Pb geochronology and REE geochemistry

Xenotime in samples TR1-07 and WOS-02 most commonly forms inclusions within chlorite, either directly at the margins of garnet or proximal to garnet within the matrix (Fig. 2b,d). Rare grains are also distributed throughout the matrix with no clear spatial association with garnet, but still associated with chlorite. BSE images show that most grains exhibit patchy zoning (Fig. 10), often separating larger homogeneous dark and light BSE response domains (Fig. 10).

5.4.1. TR1-07

Twenty-four analyses were collected from 21 individual xenotime grains in sample TR1-07. From these, 4 analyses were excluded from age calculations based on discordance and one analysis was rejected due to a high ^{204}Pb value (12 ppm). Two analyses were not considered further as they yield anomalously young ^{206}Pb/^{238}U dates of 289 ± 13 Ma and 353 ± 26 Ma, with the latter also having a highly elevated Th/U ratio (Th/U = 10.5). An additional analysis was excluded due to yielding an anomalously old ^{206}Pb/^{238}U date of 586 ± 19 Ma. The remaining 16 analyses are spread along concordia with ^{206}Pb/^{238}U dates between 497 and 436 Ma (Fig. 11a). There are no clear links between BSE zoning patterns and U–Pb age. All concordant analyses have consistent geochemical characteristics (Fig. 12a). LREE concentrations vary between 18,002–21,577 ppm. LREE slopes fall between La_N/Sm_N values of 0.0017 and 0.0035. Th/U ratios are more variable, spread between 0.41 and 3.21. There are no clear trends between xenotime geochemistry and U–Pb age, although younger analyses typically have higher Th/U ratios.

5.4.2. WOS-02

Thirteen analyses were collected from 11 individual xenotime grains in sample WOS-02. Five of these analyses were excluded from age calculations based on discordance. The remaining 8 analyses are spread along concordia with ^{206}Pb/^{238}U dates between 503 and 438 Ma (Fig. 11b). There are no clear links between BSE zoning patterns and U–Pb age. Analyses have consistent REE geochemical characteristics (Fig. 12b). LREE concentrations vary between 19,375–34,225 ppm. LREE slopes fall tightly between La_N/Sm_N values of 0.0019 and 0.0033. Th/U ratios are more variable and spread between 0.17 and 1.26. There are no discernible trends between xenotime geochemistry and U–Pb age.

5.5. 1D thermal modelling

Thermal modelling was carried out using TectoTherm, a MATLAB-based program that solves the one-dimensional, transient heat flow equation using a finite difference approximation (for details, see Appendix F in Bockmann et al., 2022). The program starts with a steady-state thermal regime with user defined boundary conditions. In the models presented here, the surface temperature was set to 15 °C and the mantle potential temperature to 1300 °C. The initial Moho depth is set to 35 km after (Kennett et al., 2011), whilst the calculated depth to the lithosphere-asthenosphere boundary is agreement with seismological estimates of ~150–250 km (Fishwick et al., 2008; Kennett and Blewett, 2012). A reduced mantle heat flow of 15 mW m^{-2} was employed based on fast seismic velocity speeds in the lower lithosphere (Neumann et al., 2000).

Model parameters were varied to best approximate the conditions experienced in the southern Curnamona Province between 840 and 400 Ma, with the goal of appraising the role of radiogenic heat production in
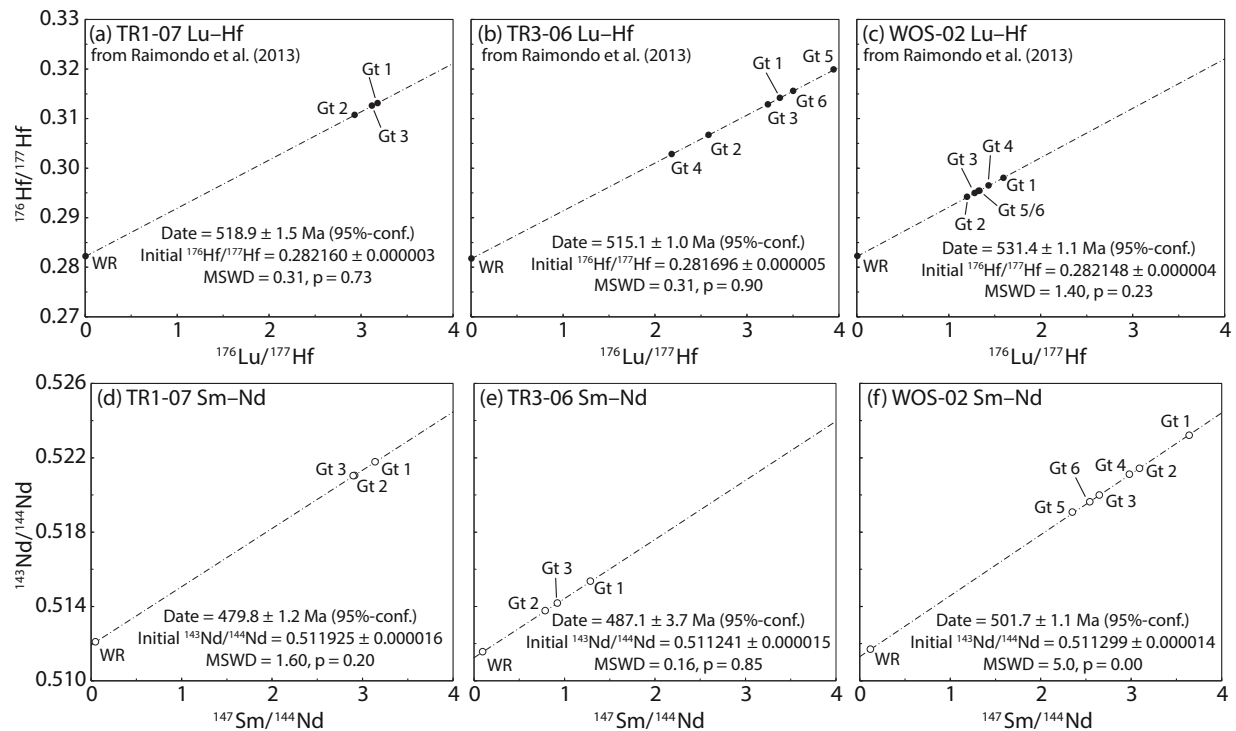
Fig. 6. Garnet Lu–Hf (a–c) and Sm–Nd (d–f) isochrons constructed from bulk garnet separates from samples TR1-07 (a,d), TR3-06 (b,e) and WOS-02 (c,f). Gt = garnet; WR = whole rock. Error bars are smaller than data point symbol size.

Table 1

Lu–Hf geochronology from samples TR1-07, TR3-06 and WOS-02, first presented in Raimondo et al. (2013). Age uncertainties are quoted at the 95% confidence interval, calculated using IsoplotR (Vermeesch, 2018). All other errors are 2SE. Chemical treatment and mass spectrometry procedures followed Anczkiewicz et al. (2004) and Thirlwall and Anczkiewicz (2004). See text for details. Gt = garnet, WR = whole rock.

| Sample label	Sample weight (mg)	Lu (ppm)	Hf (ppm)	$^{176}Lu/^{177}Hf$	$^{176}Hf/^{177}Hf$	Initial $^{176}Hf/^{177}Hf$	Date (Ma)
Sample TR1-07							
Gt 1	74.5	29.200	1.305	3.1820 ± 0.0159	0.313100 ± 0.000006		
Gt 2	74.2	29.035	1.407	2.9328 ± 0.0147	0.310705 ± 0.000005		
Gt 3	40.5	29.886	1.362	3.1192 ± 0.0156	0.312573 ± 0.000006		
WR	103.9	1.051	22.990	0.0065 ± 0.0000	0.282223 ± 0.000003	0.282160 ± 0.000003	518.9 ± 1.5
Sample TR3-06							
Gt 1	39.6	6.453	0.273	3.3602 ± 0.0168	0.314134 ± 0.000013		
Gt 2	37.9	6.702	0.368	2.5850 ± 0.0129	0.306668 ± 0.000014		
Gt 3	52.6	6.451	0.284	3.2293 ± 0.0161	0.312849 ± 0.000010		
Gt 4	54.9	6.599	0.429	2.1833 ± 0.0109	0.302812 ± 0.000008		
Gt 5	50.0	6.630	0.239	3.9442 ± 0.0197	0.319895 ± 0.000008		
Gt 6	64.4	6.900	0.280	3.5036 ± 0.0175	0.315564 ± 0.000008		
WR	96.3	0.347	9.017	0.0054 ± 0.0000	0.281750 ± 0.000005	0.281696 ± 0.000005	515.1 ± 1.0
Sample WOS-02							
Gt 1	59.7	20.540	1.823	1.5981 ± 0.0080	0.298012 ± 0.000003		
Gt 2	43.5	19.424	2.291	1.2018 ± 0.0060	0.294166 ± 0.000003		
Gt 3	50.7	20.229	2.233	1.2841 ± 0.0064	0.294956 ± 0.000005		
Gt 4	63.1	19.647	1.941	1.4350 ± 0.0072	0.296471 ± 0.000005		
Gt 5	60.0	19.467	2.084	1.3241 ± 0.0066	0.295388 ± 0.000003		
Gt 6	68.4	21.739	2.307	1.3360 ± 0.0067	0.295437 ± 0.000005		
WR	102.3	1.565	25.299	0.0087 ± 0.0000	0.282236 ± 0.000004	0.282148 ± 0.000004	531.4 ± 1.1

driving high geothermal gradient metamorphism observed in the WOSZ samples. Existing thermobarometric constraints from Dutch et al. (2005) and Clark et al. (2006) correspond to crustal depths of 18 ± 3 km, assuming a pressure gradient of 0.275 kbar km^{-1}. Models were set to run over a period of 440 Myr, beginning at 840 Ma and ending at 400 Ma. Deposition of the Adelaidean Supergroup took place between 840 and 500 Ma, with subsequent thick-skinned crustal thickening occurring at 500 Ma during the Delamerian Orogeny, followed by a period of erosion

from 480 to 400 Ma at a rate of 0.2 mm yr^{-1} (Fig. 13). The inferred depositional timing of the Adelaidean stratigraphy is based on the interpolated depositional ages defined by Preiss (2000), with the rate of deposition being a function of the depositional duration and total thickness of each Adelaidean sedimentary unit. Sedimentary thicknesses were obtained from Paul et al. (1999) and Paul et al. (2000), and further detail regarding the calculation of deposition rates is provided in Appendix E.

Table 2

Sm–Nd geochronology from samples TR1-07, TR3-06 and WOS-02. Age uncertainties are quoted at the 95% confidence interval, calculated using IsoplotR (Vermeesch, 2018). All other errors are 2SE. Chemical treatment and mass spectrometry procedures followed Anczkiewicz et al. (2004) and Thirlwall and Anczkiewicz (2004). See text for details. Gt = garnet, WR = whole rock.

| Sample label	Sample weight (mg)	Sm (ppm)	Nd (ppm)	$^{147}Sm/^{144}Nd$	$^{143}Nd/^{144}Nd$	Initial $^{143}Nd/^{144}Nd$	Date (Ma)
Sample TR1-07							
Gt 1	74.5	8.656	1.670	3.1406 ± 0.0094	0.521773 ± 0.000012		
Gt 2	74.2	8.434	1.753	2.9141 ± 0.0087	0.521038 ± 0.000017		
Gt 3	40.5	8.730	1.824	2.8990 ± 0.0087	0.521031 ± 0.000013		
WR	103.9	6.948	83.065	0.0506 ± 0.0002	0.512085 ± 0.000016	0.511925 ± 0.000016	479.8 ± 1.2
Sample TR3-06							
Gt 1	39.6	1.535	0.721	1.2890 ± 0.0039	0.515348 ± 0.000042		
Gt 2	37.9	1.668	1.277	0.7899 ± 0.0024	0.513762 ± 0.000038		
Gt 3	52.6	1.609	1.053	0.9243 ± 0.0028	0.514178 ± 0.000018		
Gt 4	54.9	n.d.	n.d.	n.d.	n.d.		
Gt 5	50.0	n.d.	n.d.	n.d.	n.d.		
Gt 6	64.4	n.d.	n.d.	n.d.	n.d.		
WR	96.3	6.744	41.756	0.0976 ± 0.0003	0.511553 ± 0.000014	0.511241 ± 0.000015	487.1 ± 3.7
Sample WOS-02							
Gt 1	59.7	9.042	1.504	3.6432 ± 0.0109	0.523206 ± 0.000012		
Gt 2	43.5	9.273	1.815	3.0947 ± 0.0093	0.521425 ± 0.000018		
Gt 3	50.7	9.352	2.137	2.6500 ± 0.0080	0.519985 ± 0.000020		
Gt 4	63.1	9.440	1.918	2.9814 ± 0.0089	0.521101 ± 0.000013		
Gt 5	60.0	9.384	2.416	2.3523 ± 0.0071	0.519062 ± 0.000017		
Gt 6	68.4	9.413	2.240	2.5445 ± 0.0076	0.519617 ± 0.000014		
WR	102.3	25.256	127.873	0.1194 ± 0.0004	0.511686 ± 0.000014	0.511299 ± 0.000014	501.7 ± 1.1
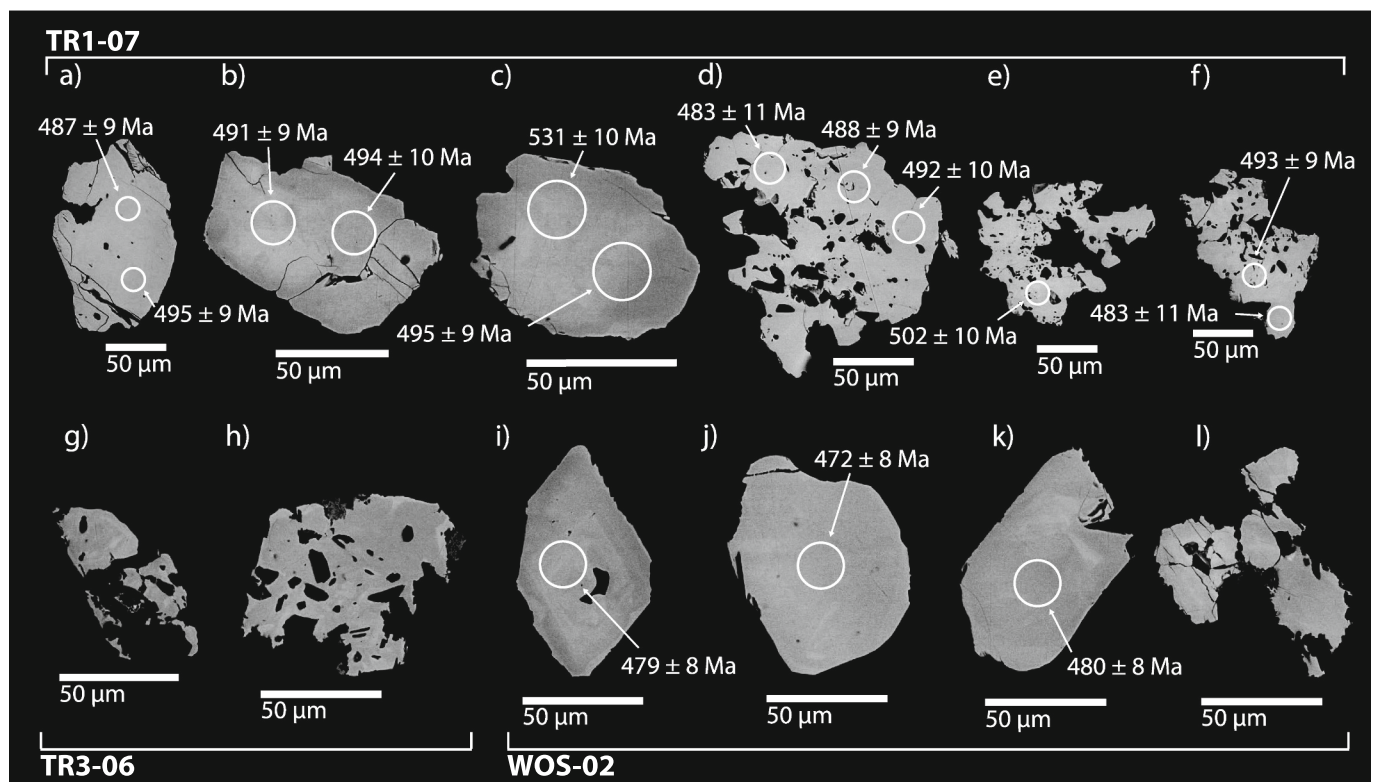
Fig. 7. Back-scattered electron images of selected monazite grains from samples TR1-07 (a–f), TR3-06 (g,h), and WOS-02 (i–l).

The physical properties of the rock types used in the thermal models, including density, thermal conductivity, specific heat capacity and radiogenic heat production, were based on values from Hasterok et al. (2018) unless otherwise stated. The heat production values for the Adelaidean and Willyama successions were back-calculated to 500 Ma and derived from a surface heat production map (Fig. 14; Appendix E) calculated using values from airborne radiometric datasets following the protocol outlined in De Vries Van Leeuwen et al. (2021). Heat production values for the Adelaidean succession vary between 0.95 and 2.09 μW m^{-3}, whereas the Willyama Supergroup was set to 2.83 μW m^{-3} based on area-averaged calculations for the dominant outcropping rock types in the region (Fig. 14b–f). Heat production values for the lower crust and mantle lithosphere were set to 0.5 and 0.02 μW m^{-3}, respectively. Thermal conductivities for Adelaidean sedimentary rocks were
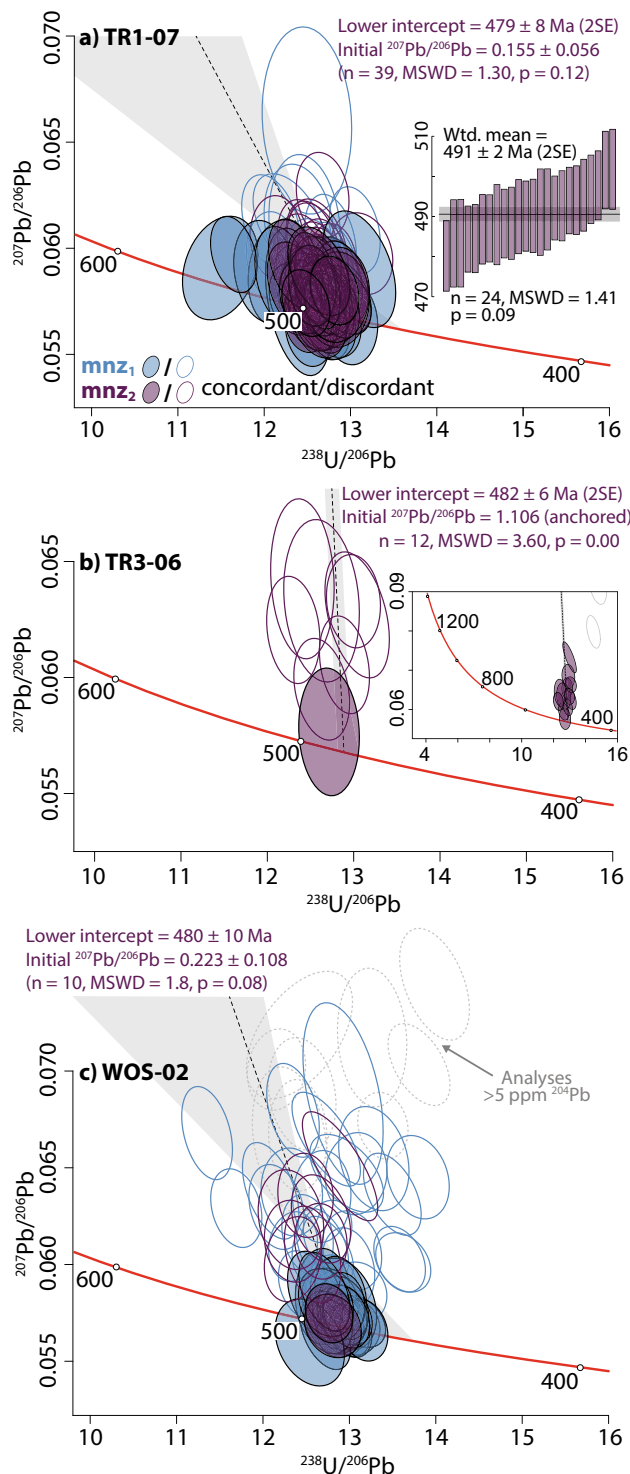
Fig. 8. Tera-Wasserburg concordia plots of monazite U–Pb geochronological data from samples TR1-07 (a), TR3-06 (b) and WOS-02 (c). Blue and purple ellipses represent analyses from the mnz_1 and mnz_2 subpopulations, respectively (see text for details). Unfilled, coloured ellipses are discordant analyses used for lower intercept age calculations, whereas grey dashed ellipses were excluded due to elevated ^{204}Pb concentrations (> 5 ppm). Inset in panel (a) depicts the distribution of $^{206}Pb/^{238}U$ dates of concordant analyses from sample TR1-07, along with the respective weighted mean age calculation. Inset in panel (b) shows a zoomed-out view of the analyses defining the lower intercept age for sample TR3-06. (For interpretation of the references to colour in this figure legend, the reader is referred to the web version of this article.)
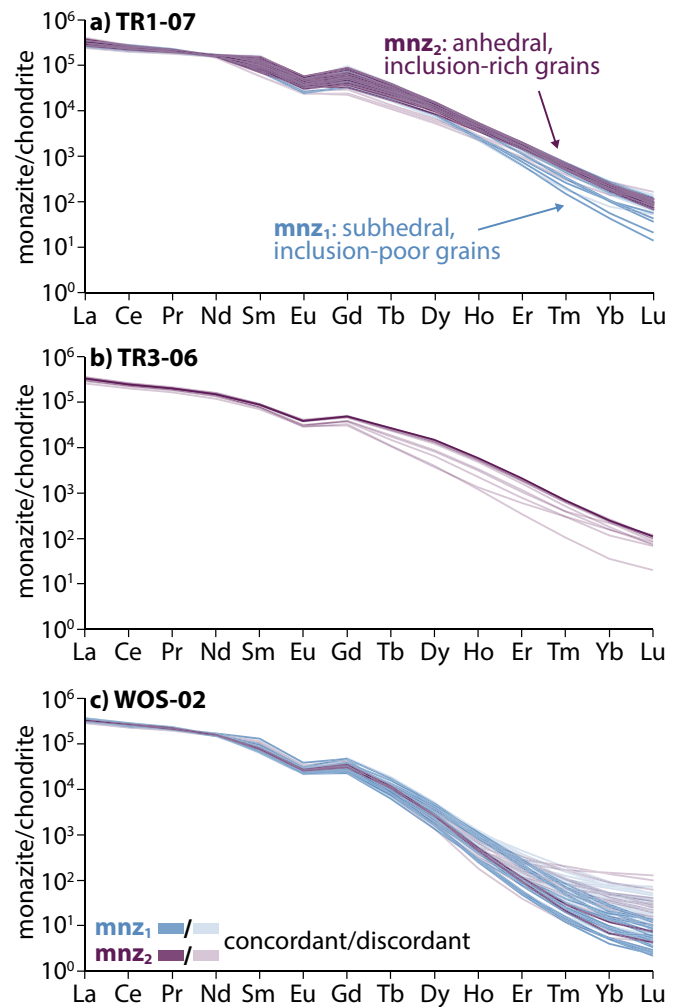

Fig. 9. Chondrite normalised REE spiderplots for monazite from samples TR1-07 (a), TR3-06 (b) and WOS-02 (c). Blue and purple lines represent analyses from the mnz_1 and mnz_2 subpopulations, respectively (see text for details). Lighter coloured lines represent discordant analyses. Chondrite normalisation follows Taylor and McLennan (1985). (For interpretation of the references to colour in this figure legend, the reader is referred to the web version of this article.)

taken from (McLaren et al., 2006), whereas the thermal conductivity of the Willyama Supergroup is approximated to 3.5 W m^{-1} K^{-1}. The lower crustal thermal conductivity was set to 2.3 W m^{-1} K^{-1} and the lithospheric mantle to 2.02 W m^{-1} K^{-1}. Thermal conductivities were set to change as a function of pressure and temperature, as depicted in Fig. 13b, with the values stated previously representing their thermal conductivities at 25 °C. Mid-to-upper crustal densities were set to 2700 kg m^{-3}, whereas the lower crust was set to 2969 kg m^{-3} and the lithospheric mantle to 3364 kg m^{-3}. The density profile changes with respect to depth as a function of thermal expansivity. For detailed explanations of the thermal and barometric dependence of physical rock properties used in TectoTherm, see Bockmann et al. (2022).

5.5.1. 1D thermal modelling results

The thermal models presented in Fig. 15 were calculated using thickness estimates for the Adelaidean and Willyama successions of 12 km and 8 km, respectively (Conor and Preiss, 2008; Dutch et al., 2005). The degree of crustal thickening during the Delamerian Orogeny was assumed to be 10% (Paul et al., 1999; Paul et al., 2000), and the erosion rate was assumed to be constant at 0.2 mm yr^{-1}. In all the models, maximum temperatures at 18 km depth (the maximum depth the
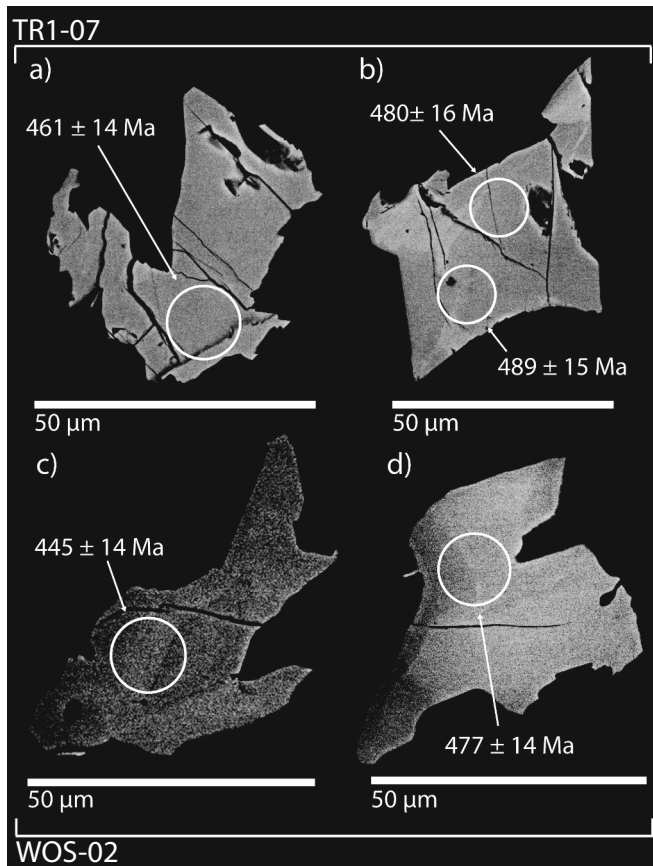
Fig. 10. Back-scattered electron images of selected xenotime grains from samples TR1-07 (a,b) and WOS-02 (c,d).

garnet–chlorite assemblages of this study are inferred to have reached) are attained at ~460 Ma, 40 Myr after thickening occurred and 20 Myr after erosion initiated.

The models presented in Fig. 15a and b investigate the effects of varying the thickness of the Adelaidean and Willyama successions on the maximum temperatures. This shows that increasing the thickness of (1) low conductivity upper-crustal rocks or (2) high heat producing basement rocks produces similar increases in crustal temperatures, with the latter also leading to steeper geothermal gradients in the upper crust. The model in Fig. 15c investigates the effect of varying the amount of crustal thickening during the Delamerian Orogeny, and shows similar results to those obtained when increasing the thickness of the Adelaidean succession (Fig. 15a). Fig. 15d demonstrates the ability for significantly higher maximum temperatures and steeper upper crustal geotherms to be attained when the radiogenic heat production of the Willyama Supergroup is increased. Similarly, Fig. 15e demonstrates the ability for steeper geotherms to be generated by increasing mantle heat flow. Fig. 15f and g show the overall thermal evolution of the crust in the southern Curnamona Province during crustal thickening and erosion. Both models assume the Adelaidean attained a maximum thickness of 12 km, and the Willyama Supergroup has a radiogenic heat production of 2.83 μW m^{-3}. Where they differ is that the minimum estimate model (Fig. 15f) assumes only 10% thickening during the Delamerian Orogeny (minimum estimate from Paul et al., 1999; Paul et al., 2000) and a thickness of 8 km for the Willyama Supergroup. The best-fit model on the other hand assumes 20% thickening during the Delamerian Orogeny (maximum estimate from Paul et al., 1999; Paul et al., 2000) and a thickness of 10 km for the Willyama Supergroup (Fig. 15g).
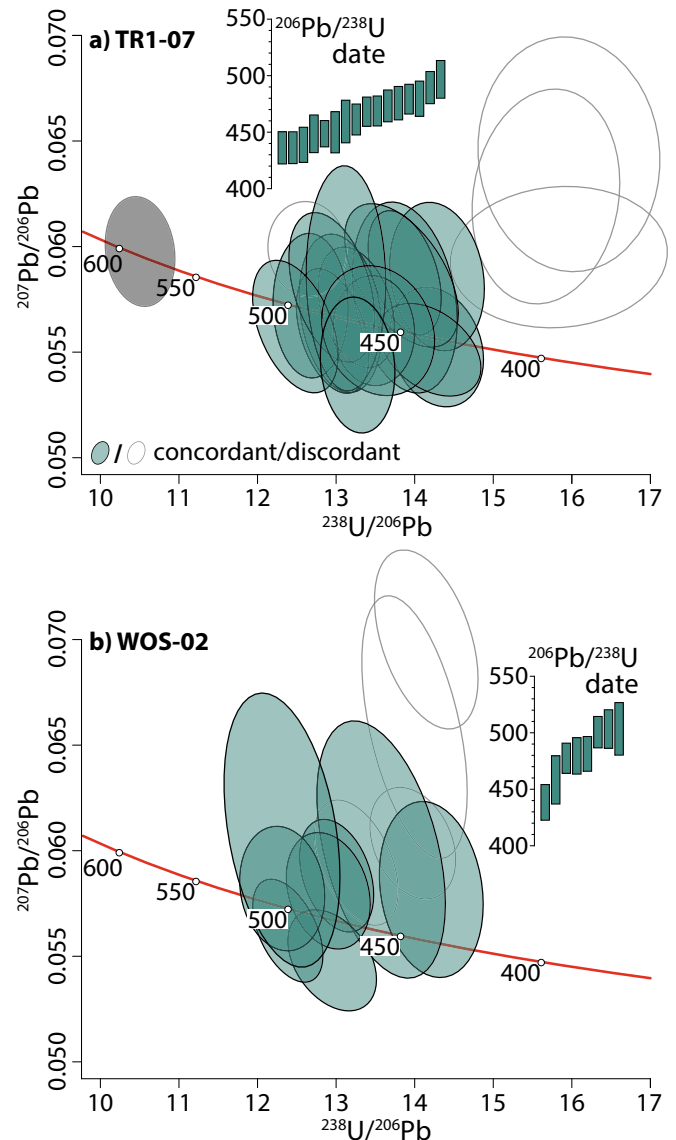
Fig. 11. Tera-Wasserburg concordia plots of xenotime U–Pb geochronological data from samples TR1-07 (a) and WOS-02 (b). Unfilled grey ellipses represent discordant analyses. The grey-filled ellipse in panel (a) represents an anomalously old analysis not considered part of the main population. Insets depict the distribution of ^{206}Pb/^{238}U dates of concordant analyses from each sample.

6. Discussion

6.1. Significance of garnet double dating results

There is a systematic ~30–40 Myr offset between garnet Lu–Hf and Sm–Nd dates obtained from each sample in this study, ranging between c. 531–515 Ma and c. 502–480 Ma, respectively. Such age differentials are often attributed to the Lu–Hf and Sm–Nd isotopic systems dating different periods of garnet growth. When garnet growth occurs following a Rayleigh Fractionation model, it is expected that Lu strongly partitions into the core during initial growth, whereas Sm concentrates towards the rim during later growth phases (e.g., Goncalves et al., 2021; Otamendi et al., 2002; Raimondo et al., 2017). Thus, Lu–Hf dates should be weighted towards the timing of incipient-to-early garnet crystallisation and Sm–Nd dates towards its final stage (e.g., Kohn, 2009; Lapen et al., 2003; Skora et al., 2006). When constructing isochrons from bulk garnet separates, the resulting Lu–Hf and Sm–Nd dates are likely to be dependent on the volume-weighted proportions of garnet core versus
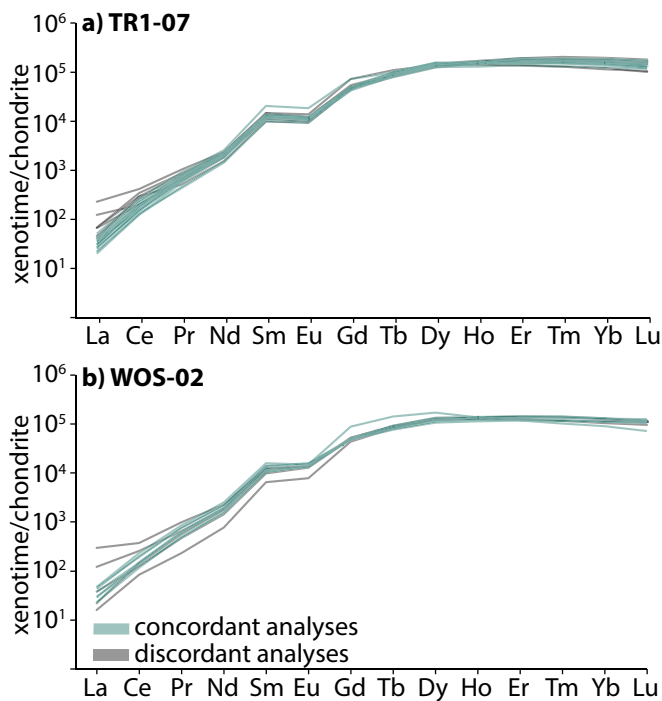
Fig. 12. Chondrite normalised REE spiderplots for xenotime from samples TR1-07 (a) and WOS-02 (b). Grey coloured lines represent discordant analyses. Chondrite normalisation follows Taylor and McLennan (1985).

rim material.

Broadly speaking, the major and trace element compositional maps from garnet in all samples analysed in this study reveal the preservation of prograde zoning patterns typically associated with Rayleigh Fractionation (e.g., Figs. 4, 5; Hollister, 1966). However, REE zoning is somewhat more complex, particularly evident in sample TR3-06 which exhibits a HREE satellite peak (Fig. 4g), suggesting that other major or accessory minerals may have influenced the supply of REEs during garnet crystallisation (e.g., Godet et al., 2022; Konrad-Schmolke et al., 2022; Raimondo et al., 2017; Rubatto et al., 2020). Irrespectively, the distribution of HREEs is strongly skewed towards garnet cores, and average Lu concentrations determined by MC–ICP–MS (Table 1) closely match those derived from core domains by LA–ICP–MS compositional mapping (Fig. 5). Following convention, this implies that Lu–Hf dates reflect the timing of early garnet growth. Notably, the average MC–ICP–MS Lu concentration for sample TR3-06 is a more intermediate value, sitting between the core and rim Lu values from LA–ICP–MS data (Fig. 5b). This sample correspondingly yields the youngest Lu–Hf age, suggesting that a larger proportion of outer core (and hence younger) material was analysed from the bulk separate.

In contrast to the HREEs, the LREEs exhibit generally flatter zoning profiles, with Sm distributions not defined by the same stark changes between core and rim domains as seen in the Lu zoning (Figs. 4 and 5). For example, in sample TR3-06 the change in Sm concentration is ~5 ppm in the core down to ~1.5 ppm in the rim, whereas Lu drops from ~25 ppm to <2 ppm. This represents a core-to-rim decrease in Sm of 300–400% compared to >12,500% for Lu. Consequently, Sm–Nd dates are likely to be much more sensitive to the volumetric proportion of core versus rim material, and hence reflect a 'volume-averaged' garnet date (Baxter and Scherer, 2013), often biased towards the timing of garnet rim formation. Generally, this suggests that Sm–Nd dates from this study place a minimum estimate on the timing of final garnet crystallisation. This is most evident in sample TR1-07, which exhibits elevated Sm in the outermost rim (Figs. 4a and 5a) and also yields the youngest Sm–Nd date, indicating the bias towards later rim growth when taking a volume-averaged date. Sample WOS-02 is an exception to this as it

yields a substantially older Sm–Nd date and has average Sm concentrations determined by MC–ICP–MS (Table 2) that correspond to core Sm values obtained from LA–ICP–MS compositional mapping (Fig. 5). This sample also has a notably broader core domain of elevated Sm concentrations that extends to within ~150 μm of the garnet rim (Figs. 4i and 5c). As a result, the bulk separate is more likely to represent a mixture with a greater proportion of core material compared to the other samples, and hence the Sm–Nd date of c. 500 Ma reflects a more intermediate phase of garnet growth.

Additional complications in interpreting Lu–Hf and Sm–Nd systematics can arise if contaminating phases contribute significant amounts of parent or daughter isotopes to the analysed fractions of garnet, particularly if these contaminating phases are not in chemical equilibrium at the time of garnet growth. The concentrations of Hf determined from MC–ICP–MS analyses (Table 1) are significantly higher than typical values for garnet (~100 ppb; Anczkiewicz et al., 2004). Hence, it is likely that there was some degree of contamination from small zircon inclusions evident on the Zr maps (Fig. 4d,h,l). Although isotopic measurements of zircon included within garnet or the matrix were not taken, it is unlikely that any zircon present would be in equilibrium with garnet given the relatively low maximum metamorphic temperatures that these rocks attained (~530 °C; Clark et al., 2006; Dutch et al., 2005). Instead, it is probable that any zircon present is inherited from either the c. 1710 Ma Basso Suite (Ashley et al., 1996; Page et al., 2005) or the c. 1580 Ma Bimbowrie Suite (Wade, 2011), which host the garnet–chlorite shear zone splays (Clark et al., 2006).

Studies have demonstrated that only small quantities of inherited zircon can have major effects on the initial $^{176}Hf/^{177}Hf$ ratio of garnet (e. g., Scherer et al., 2000). This is exacerbated by the fact that older zircons tend to become metamict, in turn increasing their solubility and making the liberation of Hf substantially easier (e.g., Gao et al., 2021). The c. 531 Ma date from sample WOS-02 is anomalously old compared to the remaining samples (c. 519–515 Ma). This sample also contains the greatest abundance of small zircon inclusions that may have been incorporated into the garnet analysis (Fig. 4l), and the highest Hf values measured by MC–ICP–MS (Table 1). It is therefore likely that sample WOS-02 has an apparent age older than its true age, and some caution should be exercised in extending the timing of early garnet growth as far back as c. 531 Ma.

Zircon inclusions are also present in sample TR1-07 and to a lesser extent sample TR3-06, but in both cases are much larger grains than in WOS-02 and would likely have been mechanically separated from garnet during crushing and sample preparation. The elevated Hf concentrations observed in TR1-07, and to a lesser extent TR3-06, may therefore be attributed to contamination from other matrix minerals containing trace amounts of Hf. Given that these matrix minerals would have been in chemical equilibrium with garnet during metamorphism, any Hf contributed from their dissolution would share the same initial $^{176}Hf/^{177}Hf$ ratio as garnet, and would likely only act to reduce the precision of the determined Lu–Hf dates due to lowering the $^{176}Lu/^{177}Hf$ ratios of the garnet aliquots (e.g., Raimondo et al., 2013). Zr-rich veins and diffuse zones of Zr enrichment, which are correspondingly enriched in Hf, are seen dissecting garnets from each sample (Fig. 4). These features are dominantly comprised of goethite, interpreted to have formed during low-T alteration. Any goethite present in the garnet separates used for MC–ICP–MS analysis would have been removed during the dissolution and leaching procedures applied (Anczkiewicz and Thirlwall, 2003). Our preference is therefore to interpret c. 519 Ma from sample TR1-07 as the most likely timing of initial garnet growth, and c. 515 Ma from sample TR3-06 as an intermediate phase of garnet growth as argued above.

6.2. Monazite and xenotime U–Pb geochronology

Monazite and xenotime U–Pb geochronology are used to contextualise garnet geochronology and add further constraints to the
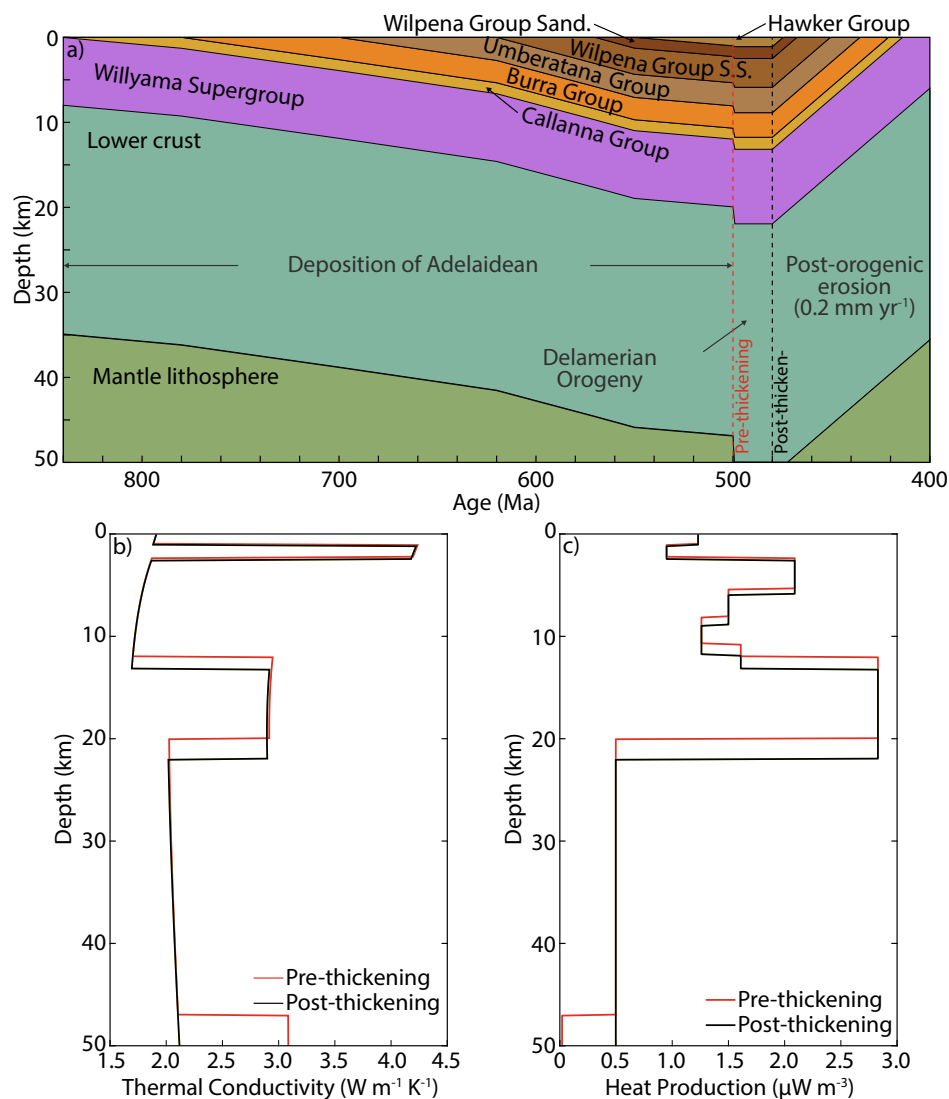
Fig. 13. (a) Generalised model setup showing the thickness and time-space distribution of rock units used to construct the thermal models presented in Fig. 15. Panels (b) and (c) show the thermal conductivity and heat production profiles for the pre-thickening and post-thickening phases of the generalised model shown in (a). Stratigraphic thicknesses of the Adelaidean Supergroup are based on palynspastic reconstructions of Paul et al. (1999) and Paul et al. (2000).

timing and duration of metamorphism in the southern Curnamona Province. Monazite exists in two morphological styles throughout the samples analysed. The first of these (mnz_1) comprises typically subhedral grains devoid of inclusions (e.g., Fig. 7a–c,i–k). They record a spread of concordant dates from 516 to 472 Ma, along with two older dates of 538 and 531 Ma (Fig. 8). Monazite belonging to mnz_1 typically exhibits patchy zoning in BSE images (Fig. 7) and variable REE compositions (Fig. 9). Due to the patchy zoning and small grain size of mnz_1, it was not possible to confidently analyse individual zones. Mixing of different compositional domains may therefore explain the observed spread in U–Pb dates along concordia and variable REE signatures. The second style of monazite (mnz_2) comprises anhedral, inclusion-rich grains (e.g., Fig. 7d–h,l) that are unzoned in BSE images and have consistent REE compositions. Concordant analyses of mnz_2 range between 502 and 480 Ma (Fig. 8). When discordant analyses from the mnz_2 population are included, a well-defined discordia emerges with a lower intercept of c. 480 Ma in each sample (Fig. 8).

The anhedral inclusion-rich morphology of mnz_2 grains may indicate that they formed through coupled dissolution–precipitation (e.g., Harlov et al., 2011; Seydoux-Guillaume et al., 2002; Williams et al., 2011). This process would have likely involved the compositional homogenisation of mnz_1, resulting in the tighter clustering of REE geochemistry

and U–Pb dates observed in the mnz_2 population. The REE geochemistry of mnz_2 is broadly equivalent to that of mnz_1, consistent with the interpretation that mnz_2 formed via the dissolution and re-precipitation of mnz_1 rather than an external source of REE and P. Incomplete dissolution of mnz_1 may have also contributed to the apparent spread of U–Pb dates in the mnz_1 population. In sum, the monazite geochronology suggests a protracted history of monazite growth commencing by at least c. 516 Ma, followed by fluid-induced resetting at approximately c. 490–480 Ma. This closely corresponds to the metamorphic evolution established by garnet Lu–Hf and Sm–Nd geochronology, with initial monazite growth closely following the first appearance of garnet, and both garnet and monazite growth or recrystallisation persisting until c. 480 Ma.

Xenotime in samples TR1-07 and WOS-02 are predominantly found as inclusions within chlorite partially replacing garnet (Fig. 2b,d), with the Y + HREE liberated from garnet breakdown inferred to have facilitated xenotime growth (e.g., Foster et al., 2004). This observation implies that xenotime is effectively dating the timing of garnet breakdown. Concordant xenotime dates vary between 503 and 436 Ma, implying that garnet breakdown was protracted. Garnet in both samples varies from intact to near-total replacement by chlorite (Fig. 2d,e), suggesting that garnet stability varied between local equilibrium volumes and there
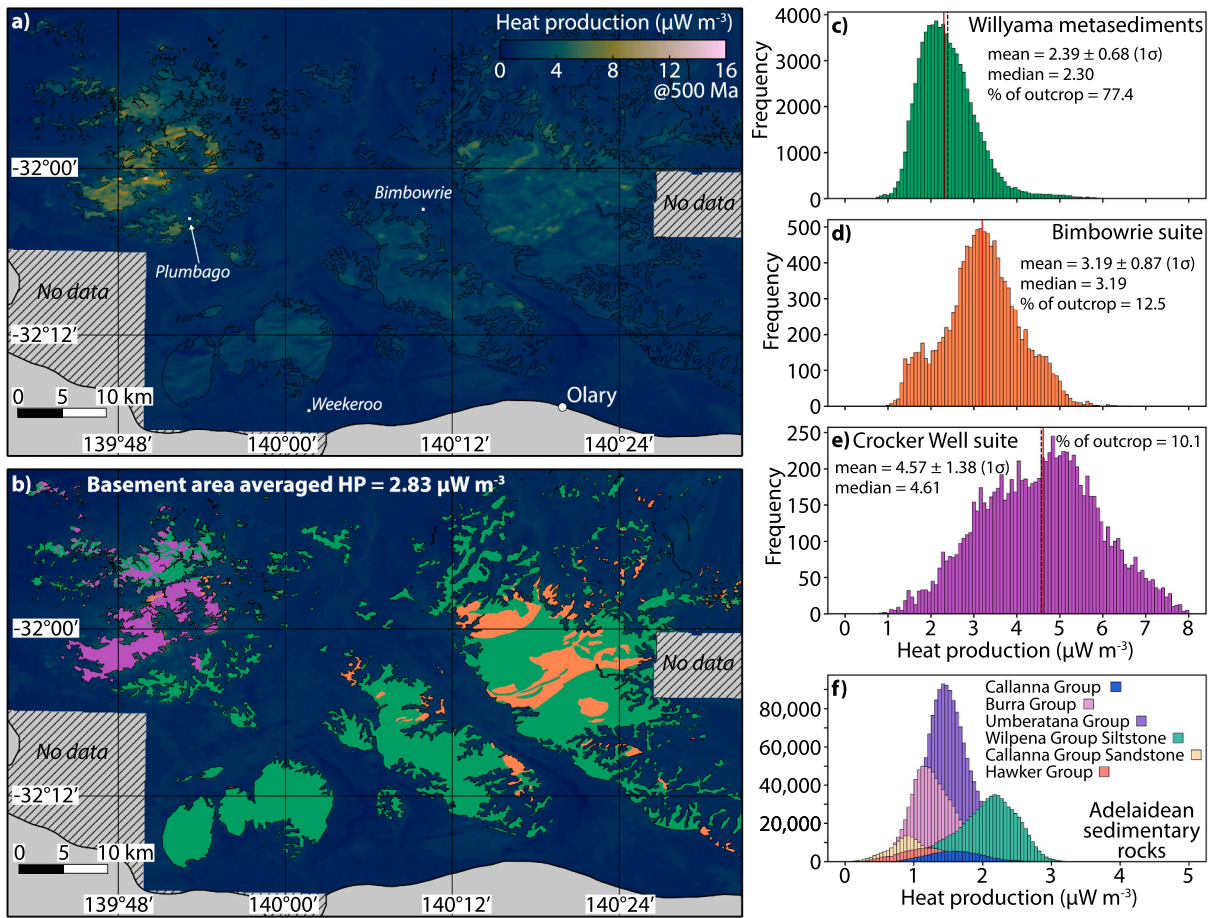
Fig. 14. (a) Heat production map of the Willyama Inliers in the southern Curnamona Province calculated at 500 Ma; (b) Superimposed heat production map as presented in panel (a), showing the extents of the Willyama metasediments (green), Bimbowrie Suite (orange), and the Crocker Well Suite (pink); (c–f) Histograms showing the heat production distribution of each of the rock units used to construct the thermal models presented in Fig. 15. Heat production values for the Adelaidean sedimentary rocks are provided in Appendix E. (For interpretation of the references to colour in this figure legend, the reader is referred to the web version of this article.)
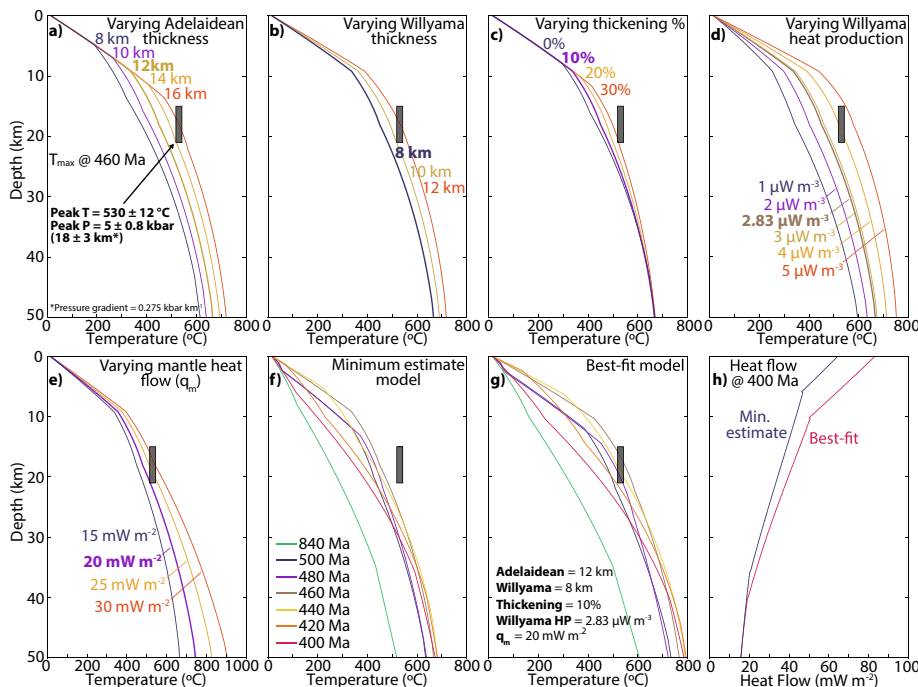
Fig. 15. One-dimensional thermal models constructed to best approximate the metamorphic conditions experienced in the southern Curnamona Province between 840 and 400 Ma. Panels (a–e) use the default model parameters outlined in the text, with the following parameters being varied as listed and the maximum temperature attained at 460 Ma presented for comparison (grey box): (a) thickness of the Adelaidean succession; (b) thickness of the Willyama Supergroup; (c) percentage of thickening; (d) Willyama radiogenic heat production rate; and (e) mantle heat flow. Panels (f) and (g) depict the minimum estimate and best-fit models discussed in the text, with panel (h) showing the variation in heat flow between these two models at 400 Ma.

was limited chemical communication throughout the rock at the thin section scale. The patchy nature of garnet breakdown also supports that the garnet–chlorite shear zone splays remained a chemically closed system for the duration of metamorphism (e.g.,Clark et al., 2006; Raimondo et al., 2013). If large volumes of exogenous fluids had at any time fluxed the system, it is unlikely that such small-scale chemical heterogeneities would persist, and instead garnet would exhibit ubiquitous breakdown textures. The spatially focused Delamerian metamorphic imprint in the WOSZ is hence interpreted to reflect the increased bulk-rock reactivity of the hydrated shear zone assemblages imparted by an inherited history of near-surface alteration along permeable fault panels (Clark et al., 2006; Raimondo et al., 2013). This contrasts against the more refractory wall rocks of the Willyama Supergroup (comprising metasedimentary and granitic rocks that previously underwent a cycle of HT–LP metamorphism during the Olarian Orogeny), which were not rehydrated at near-surface conditions and thus remained metastable.

6.3. Towards a petrochronological model for the WOSZ

Linking U–Pb dates from accessory minerals to garnet enables the development of a coherent petrogenetic model for the garnet–chlorite splays of the Walter-Outalpa Shear Zone, where dates derived from accessory minerals can be linked directly to the bulk silicate assemblage, and vice versa. To effectively do so, context for the two generations of monazite and the protracted period of xenotime growth needs to be found in the garnet Lu–Hf and Sm–Nd dates previously discussed. Early monazite belonging to mnz_1 records U–Pb dates between 516 and 472 Ma, with two considerably older analyses yielding dates of 538 and 531 Ma. As stated above, the oldest analyses on the concordant spread at c. 516 Ma closely coincide with the timing of early garnet growth inferred from Lu–Hf dating (c. 519 Ma). Monazite from the mnz_2 population occupy a much tighter spread of c. 490–480 Ma, interpreted to reflect isotopic resetting of existing monazite from the mnz_1 population via coupled dissolution–precipitation. This timing agrees with the Sm–Nd garnet dates proposed to be biased towards the timing of rim growth, although not necessarily constraining the timing of final garnet crystallisation. The coincidence between the formation of garnet rims and of mnz_2 potentially signals that garnet growth was facilitated by the up-temperature breakdown of chlorite, which in turn would have liberated fluid to drive the coupled dissolution–precipitation of mnz_1 to form mnz_2. Xenotime, which yields a large spread of dates between 503 and 436 Ma, is then considered to have formed as the product of subsequent garnet breakdown. Although some individual dates are older than c. 480 Ma, determined by mnz_2 U–Pb and garnet Sm–Nd dates, reflects the earliest plausible timing of final garnet growth, most xenotime analyses yield younger dates. This suggests that garnet breakdown occurred between c. 480–440 Ma, likely over a protracted period facilitated by highly localised reactions and decreasing metamorphic pressures and temperatures during exhumation.

6.4. Thermal drivers for metamorphism

Combining the temporal framework outlined above with the preservation of prograde garnet zoning profiles in all samples (Figs. 3 and 4; Hollister, 1966) suggests that prograde-to-peak metamorphism spanned the period c. 519–480 Ma. This c. 39 Myr period was characterised by an apparent geothermal gradient of ~105 °C kbar^{-1}, with rocks of the Walter-Outalpa Shear Zone reaching maximum temperatures of ~530 °C at 5 kbar (Clark et al., 2006; Dutch et al., 2005). Typically, occurrences of high geothermal gradient metamorphism in the Adelaide Superbasin (Fig. 1) have been highly localised, restricted to the Adelaidean Supergroup sedimentary rocks, and can be attributed to advective heating via granitic magmas generated during the Delamerian Orogeny (e.g., Foden et al., 2006; Greenfield et al., 2011; Johnson et al., 2016; Sandiford et al., 1992; Sandiford et al., 1995). However, in the southern Curnamona Province there are no significant occurrences of

Delamerian-aged magmatic rocks. Furthermore, the contrasting thick- and thin-skinned deformational styles during the Delamerian Orogeny have been correlated with differences in the stratigraphic thickness of the Adelaidean Supergroup, where regions blanketed by a thicker succession tend to exhibit more basement involvement (Paul et al., 1999; Paul et al., 2000; Sandiford et al., 1998b). Sandiford et al. (1998b) have attributed this difference in deformation style to the thermal insulation and greater depth-to-basement provided by an increasingly thick sedimentary succession, the consequence of which is to significantly elevate temperatures at depth, thus rheologically weakening the crust and facilitating basement deformation. As such, we favour a scenario where crustal geotherms already elevated due to high radiogenic heat production in the Willyama Supergroup (Fig. 14) were propagated to greater depths during crustal thickening, further elevating maximum crustal temperatures (e.g., Clark et al., 2011).

1D thermal modelling was carried out to investigate whether radiogenic heat production alone could drive the high thermal gradient metamorphism recorded in this study (Fig. 15). A minimum crustal thickening estimate of 10% during the Delamerian Orogeny (Paul et al., 1999), coupled with a minimum 8 km thickness of the Willyama Supergroup (Conor and Preiss, 2008) and a reduced mantle heat flow of 15 mW m^{-2} (Neumann et al., 2000), fails to replicate the temperature conditions attained in the Walter-Outalpa Shear Zone (Fig. 15f). However, with only moderate increases to these minimum estimates (crustal thickening to 20%, Willyama Supergroup thickness to 10 km, and mantle heat flow to 20 mW m^{-2}), the maximum *P–T* conditions stated by Dutch et al. (2005) and Clark et al. (2006) are able to be replicated (Fig. 15g). These increases are well within the range of plausible values for these parameters, given that: (1) Paul et al. (1999) and Paul et al. (2000) state that the potential range of crustal thickening experienced during the Delamerian Orogeny was 10–20%; (2) Conor and Preiss (2008) suggest an 8 km thickness for the Willyama Supergroup is a minimum thickness based on current exposures, with seismic evidence suggesting a potentially greater maximum thickness (Goleby et al., 2006); and (3) accounting for the secular cooling of Earth it is likely that mantle heat flow was higher at 500 Ma than the present-day mantle heat flow value of 15 mW m^{-2} based on seismic velocity constraints (Neumann et al., 2000). Furthermore, surface heat flow values calculated at 400 Ma (after exhumation to approximate present-day crustal levels) for both the minimum estimate and best-fit models are 64 and 82 mW m^{-2}, respectively (Fig. 15h). The latter closely corresponds to measured heat flow values from drillholes across the central and southern Curnamona Province, which yield values between 79 and 103 mW m^{-2} (Jones et al., 2011).

With the results of thermal modelling corroborating our petrochronological data, we conclude that the observed high geothermal gradient metamorphism in the WOSZ was generated via the burial and subsequent thickening of the Willyama Supergroup due to its elevated radiogenic heat production. This highlights the importance of the thermal structure of the crust inboard from active tectonic margins in facilitating reactivation and reworking and producing polymetamorphic records. Hotter and weaker crust is more amenable to structural reworking due to its rheological contrast (e.g., Sandiford et al., 1998b), leading to regions of crust typically isolated from far-field stresses becoming focal points for renewed deformation and metamorphism. Similar scenarios exist in the northwestern Curnamona Province and central Australia, where regions of crust hosting significant volumes of thermally energetic basement rocks are characterised by repeated and prolonged periods of tectonic reactivation (e.g., Alessio et al., 2020; De Vries Van Leeuwen et al., 2021; McLaren et al., 2006; Prent et al., 2020; Raimondo et al., 2014; Sandiford and Hand, 1998). The persistence of thermally anomalous crust may therefore be the fundamental driver for the multiply overprinted metamorphic histories that define these terranes.

7. Conclusions

Garnet Lu–Hf and Sm–Nd geochronology and monazite U–Pb dating reveal a prolonged period of high geothermal gradient metamorphism in the Walter-Outalpa Shear Zone between c. 519–480 Ma, followed by fluid-rock interaction and garnet breakdown between c. 480–440 Ma based on xenotime U–Pb dating. Thermal modelling supports the argument that high geothermal gradient metamorphism in the southern Curnamona Province was driven by the elevated radiogenic heat production hosted in the basement rocks of Willyama Supergroup. Burial of these high heat producing basement rocks beneath lower conductivity sedimentary rocks, followed by modest crustal thickening, is sufficient to generate the *P–T* conditions associated with peak metamorphism.

Declaration of Competing Interest

The authors declare the following financial interests/personal relationships which may be considered as potential competing interests.
Co-author listed on the Editorial Board of the journal - Chris Clark.

Acknowledgements

Appendix A. Supplementary data

Supplementary data to this article can be found online at https://doi.org/10.1016/j.lithos.2023.107137.

References

Alessio, K.L., Hand, M., Kelsey, D.E., Williams, M.A., Morrissey, L.J., Barovich, K., 2018. Conservation of deep crustal heat production. Geology 46, 335–338.

Alessio, K.L., Hand, M., Hasterok, D., Morrissey, L.J., Kelsey, D.E., Raimondo, T., 2020. Thermal modelling of very long-lived (>140 Myr) high thermal gradient metamorphism as a result of radiogenic heating in the Reynolds Range, Central Australia. Lithos 352-353, 105280.

Anczkiewicz, R., Thirlwall, M.F., 2003. Improving precision of Sm-Nd garnet dating by H2SO4 leaching: a simple solution to the phosphate inclusion problem. Geol. Soc. Lond., Spec. Publ. 220, 83.

Anczkiewicz, R., Platt, J.P., Thirlwall, M.F., Wakabayashi, J., 2004. Franciscan subduction off to a slow start: evidence from high-precision Lu–Hf garnet ages on high grade-blocks. Earth Planet. Sci. Lett. 225, 147–161.

Ashley, P.M., Cook, N.D.J., Fanning, C.M., 1996. Geochemistry and age of metamorphosed felsic igneous rocks with A-type affinities in the Willyama Supergroup, Olary Block, South Australia, and implications for mineral exploration. Lithos 38, 167–184.

Baxter, E.F., Scherer, E.E., 2013. Garnet Geochronology: Timekeeper of Tectonometamorphic Processes. Elements 9, 433–438.

Bockmann, M.J., Hand, M., Morrissey, L.J., Payne, J.L., Hasterok, D., Teale, G., Conor, C., 2022. Punctuated geochronology within a sustained high-temperature thermal regime in the southeastern Gawler Craton. Lithos 430-431, 106860.

Clark, C., Hand, M., 2010. Decoding Mesoproterozoic and Cambrian metamorphic events in Willyama Complex metapelites through the application of Sm–Nd garnet geochronology and P–T pseudosection analysis. Gondwana Res. 17, 59–74.

Clark, C., Hand, M., Faure, K., Mumm, A.S., 2006. Up-temperature flow of surface-derived fluids in the mid-crust: the role of pre-orogenic burial of hydrated fault rocks. J. Metamorph. Geol. 24, 367–387.

Clark, C., Fitzsimons, I.C., Healy, D., Harley, S.L., 2011. How does the continental crust get really hot? Elements 7, 235–240.

Clarke, G.L., Burg, J.P., Wilson, C.J.L., 1986. Stratigraphic and structural constraints on the proterozoic tectonic history of the Olary Block, South Australia. Precambrian Res. 34, 107–137.

Clarke, G.L., Guiraud, M., Powell, R., Burg, J.P., 1987. Metamorphism in the Olary Block, South Australia: compression with cooling in a Proterozoic fold belt. J. Metamorph. Geol. 5, 291–306.

Collins, W.J., 2002. Hot orogens, tectonic switching, and creation of continental crust. Geology 30, 535–538.

Conor, C.H.H., Preiss, W.V., 2008. Understanding the 1720–1640Ma Palaeoproterozoic Willyama Supergroup, Curnamona Province, Southeastern Australia: Implications for tectonics, basin evolution and ore genesis. Precambrian Res. 166, 297–317.

De Vries Van Leeuwen, A.T., Hand, M., Morrissey, L.J., Raimondo, T., 2021. Th–U powered metamorphism: thermal consequences of a chemical hotspot. J. Metamorph. Geol. 39, 541–565.

De Vries Van Leeuwen, A.T., Morrissey, L.J., Raimondo, T., Hand, M., 2022. Prolonged high thermal gradient metamorphism in the Curnamona Province, south-Central Australia, during the latter stages of Nuna assembly. Precambrian Res. 378, 106775.

Dutch, R.A., Hand, M., Clark, C., 2005. Cambrian reworking of the southern Australian Proterozoic Curnamona Province: constraints from regional shear-zone systems. J. Geol. Soc. 162, 763.

Dymoke, P., Sandiford, M., 1992. Phase relationships in Buchan facies series pelitic assemblages: calculations with application to andalusite-staurolite parageneses in the Mount Lofty Ranges, South Australia. Contrib. Mineral. Petrol. 110, 121–132.

Fishwick, S., Heintz, M., Kennett, B.L.N., Reading, A.M., Yoshizawa, K., 2008. Steps in lithospheric thickness within eastern Australia, evidence from surface wave tomography. Tectonics 27.

Foden, J., Elburg, M.A., Dougherty-Page, J., Burtt, A., 2006. The timing and Duration of the Delamerian Orogeny: Correlation with the Ross Orogen and Implications for Gondwana Assembly. J. Geol. 114, 189–210.

Foden, J., Elburg, M., Turner, S., Clark, C., Blades, M.L., Cox, G., Collins, A.S., Wolff, K., George, C., 2020. Cambro-Ordovician magmatism in the Delamerian orogeny: Implications for tectonic development of the southern Gondwanan margin. Gondwana Res. 81, 490–521.

Forbes, C.J., Betts, P.G., Giles, D., Weinberg, R., 2008. Reinterpretation of the tectonic context of high-temperature metamorphism in the Broken Hill Block, NSW, and implications on the Palaeo- to Meso-Proterozoic evolution. Precambrian Res. 166, 338–349.

Foster, G., Parrish, R.R., Horstwood, M.S.A., Chenery, S., Pyle, J., Gibson, H.D., 2004. The generation of prograde P–T–t points and paths; a textural, compositional, and chronological study of metamorphic monazite. Earth Planet. Sci. Lett. 228, 125–142.

Gao, P., Yakymchuk, C., Zhang, J., Yin, C., Qian, J., Li, Y., 2021. Preferential dissolution of uranium-rich zircon can bias the hafnium isotope compositions of granites. Geology 50, 336–340.

Giles, D., Betts, P.G., Lister, G.S., 2004. 1.8–1.5-Ga links between the North and South Australian Cratons and the Early–Middle Proterozoic configuration of Australia. Tectonophysics 380, 27–41.

Glen, R.A., 2013. Refining accretionary orogen models for the Tasmanides of eastern Australia. Aust. J. Earth Sci. 60, 315–370.

Godet, A., Raimondo, T., Guilmette, C., 2022. Atoll garnet: insights from LA-ICP-MS trace element mapping. Contrib. Mineral. Petrol. 177, 57.

Goleby, B.R., Korsch, R.J., Fomin, T., Conor, C.H.H., Preiss, W.V., Robertson, R.S., Burtt, A.C., 2006. The 2003–2004 Curnamona Province Seismic Survey: Workshop Notes. Geoscience Australia.

Goncalves, P., Raimondo, T., Paquette, J.-L., de Souza, Santos, de Oliveira, J., 2021. Garnet as a monitor for melt–rock interaction: Textural, mineralogical, and compositional evidence of partial melting and melt-driven metasomatism. J. Metamorph. Geol. 39, 617–648.

Greenfield, J.E., Musgrave, R.J., Bruce, M.C., Gilmore, P.J., Mills, K.J., 2011. The Mount Wright Arc: a Cambrian subduction system developed on the continental margin of East Gondwana, Koonenberry Belt, eastern Australia. Gondwana Res. 19, 650–669.

Harlov, D.E., Wirth, R., Hetherington, C.J., 2011. Fluid-mediated partial alteration in monazite: the role of coupled dissolution–reprecipitation in element redistribution and mass transfer. Contrib. Mineral. Petrol. 162, 329–348.

Hasterok, D., Gard, M., Webb, J., 2018. On the radiogenic heat production of metamorphic, igneous, and sedimentary rocks. Geosci. Front. 9, 1777–1794.

Hollister, L.S., 1966. Garnet Zoning: an Interpretation based on the Rayleigh Fractionation Model. Science 154, 1647–1651.

Hyndman, R.D., Currie, C.A., Mazzotti, S.P., 2005. Subduction zone backarcs, mobile belts, and orogenic heat. GSA Today 15, 4–10.

Johnson, E.L., Phillips, G., Allen, C.M., 2016. Ediacaran–Cambrian basin evolution in the Koonenberry Belt (eastern Australia): Implications for the geodynamics of the Delamerian Orogen. Gondwana Res. 37, 266–284.

Jones, T., Kirkby, A., Gerner, E., Weber, R., 2011. Heat Flow Determinations for the Australian continent: Release 2. Geosci. Australia 24.

Kennett, B.L., Blewett, R.S., 2012. Lithospheric framework of Australia. Episodes 35, 9–22.

Kennett, B.L.N., Salmon, M., Saygin, E., AusMoho-Working-Group, 2011. AusMoho: the variation of Moho depth in Australia. Geophys. J. Int. 187, 946–958.

Kohn, M.J., 2009. Models of garnet differential geochronology. Geochim. Cosmochim. Acta 73, 170–182.

Kohn, M.J., Engi, M., Lanari, P., 2019. Petrochronology: Methods and Applications. De Gruyter.

Konrad-Schmolke, M., Halama, R., Chew, D., Heuzé, C., De Hoog, J., Ditterova, H., 2022. Discrimination of thermodynamic and kinetic contributions to the heavy rare earth element patterns in metamorphic garnet. J. Metamorp. Geol. https://doi.org/10.1111/jmg.12703.

Korhonen, F.J., Johnson, S.P., 2015. The role of radiogenic heat in prolonged intraplate reworking: the Capricorn Orogen explained? Earth Planet. Sci. Lett. 428, 22–32.

Lanari, P., Vidal, O., De Andrade, V., Dubacq, B., Lewin, E., Grosch, E.G., Schwartz, S., 2014. XMapTools: a MATLAB©-based program for electron microprobe X-ray image processing and geothermobarometry. Comput. Geosci. 62, 227–240.

Lapen, T.J., Johnson, C.M., Baumgartner, L.P., Mahlen, N.J., Beard, B.L., Amato, J.M., 2003. Burial rates during prograde metamorphism of an ultra-high-pressure terrane: an example from Lago di Cignana, western Alps, Italy. Earth Planet. Sci. Lett. 215, 57–72.

Lloyd, J.C., Blades, M.L., Counts, J.W., Collins, A.S., Amos, K.J., Wade, B.P., Hall, J.W., Hore, S., Ball, A.L., Shahin, S., Drabsch, M., 2020. Neoproterozoic geochronology and provenance of the Adelaide Superbasin. Precambrian Res. 350, 105849.

Mahan, K.H., Goncalves, P., Williams, M.L., Jercinovic, M.J., 2006. Dating metamorphic reactions and fluid flow: application to exhumation of high-P granulites in a crustal-scale shear zone, western Canadian Shield. J. Metamorph. Geol. 24, 193–217.

McLaren, S., Powell, R., 2014. Magmatism, orogeny and the origin of high-heat-producing granites in Australian Proterozoic terranes. J. Geol. Soc. 171, 149–152.

McLaren, S., Sandiford, M., Powell, R., Neumann, N., Woodhead, J.O.N., 2006. Palaeozoic Intraplate Crustal Anatexis in the Mount Painter Province, South Australia: timing, thermal Budgets and the Role of Crustal Heat Production. J. Petrol. 47, 2281–2302.

Musgrave, R.J., 2015. Oroclines in the Tasmanides. J. Struct. Geol. 80, 72–98.

Neumann, N., Sandiford, M., Foden, J., 2000. Regional geochemistry and continental heat flow: implications for the origin of the south Australian heat flow anomaly. Earth Planet. Sci. Lett. 183, 107–120.

Otamendi, J.E., de la Rosa, J.S.D., Douce, A.E.P.O., Castro, A., 2002. Rayleigh fractionation of heavy rare earths and yttrium during metamorphic garnet growth. Geology 30, 159–162.

Page, R.W., Conor, C.H.H., Stevens, B.P.J., Gibson, G.M., Preiss, W.V., Southgate, P.N., 2005. Correlation of Olary and Broken Hill Domains, Curnamona Province: possible Relationship to Mount Isa and Other North Australian Pb-Zn-Ag-Bearing Successions. Econ. Geol. 100, 663–676.

Paul, E., Flöttmann, T., Sandiford, M., 1999. Structural geometry and controls on basement-involved deformation in the northern Flinders Ranges, Adelaide Fold Belt, South Australia. Aust. J. Earth Sci. 46, 343–354.

Paul, E., Sandiford, M., Flöttmann, T., 2000. Structural geometry of a thick-skinned fold-thrust belt termination: the Olary Block in the Adelaide Fold Belt, South Australia. Aust. J. Earth Sci. 47, 281–289.

Preiss, W.V., 2000. The Adelaide Geosyncline of South Australia and its significance in Neoproterozoic continental reconstruction. Precambrian Res. 100, 21–63.

Prent, A.M., Beinlich, A., Raimondo, T., Kirkland, C.L., Evans, N.J., Putnis, A., 2020. Apatite and monazite: an effective duo to unravel superimposed fluid-flow and deformation events in reactivated shear zones. Lithos 376-377, 105752.

Pyle, J.M., Spear, F.S., 1999. Yttrium zoning in garnet: coupling of major and accessory phases during metamorphic reactions. Geol. Mater. Res. 1, 1–49.

Raimondo, T., Clark, C., Hand, M., Cliff, J., Anczkiewicz, R., 2013. A simple mechanism for mid-crustal shear zones to record surface-derived fluid signatures. Geology 41, 711–714.

Raimondo, T., Hand, M., Collins, W.J., 2014. Compressional intracontinental orogens: Ancient and modern perspectives. Earth Sci. Rev. 130, 128–153.

Raimondo, T., Payne, J.L., Wade, B.P., Lanari, P., Clark, C., Hand, M., 2017. Trace element mapping by LA-ICP-MS: assessing geochemical mobility in garnet. Contrib. Mineral. Petrol. 172, 17.

Rubatto, D., 2002. Zircon trace element geochemistry: partitioning with garnet and the link between U–Pb ages and metamorphism. Chem. Geol. 184, 123–138.

Rubatto, D., Burger, M., Lanari, P., Hattendorf, B., Schwarz, G., Neff, C., Keresztes Schmidt, P., Hermann, J., Vho, A., Günther, D., 2020. Identification of growth mechanisms in metamorphic garnet by high-resolution trace element mapping with LA-ICP-TOFMS. Contrib. Mineral. Petrol. 175, 61.

Rutherford, L., Hand, M., Mawby, J., 2006. Delamerian-aged metamorphism in the southern Curnamona Province, Australia: implications for the evolution of the Mesoproterozoic Olarian Orogeny. Terra Nova 18, 138–146.

Sandiford, M., Hand, M., 1998. Controls on the locus of intraplate deformation in Central Australia. Earth Planet. Sci. Lett. 162, 97–110.

Sandiford, M., Foden, J., Zhou, S., Turner, S., 1992. Granite genesis and the mechanics of convergent orogenic belts with application to the southern Adelaide Fold Belt. Earth Environ. Sci. Trans. Royal Soc. Edin. 83, 83–93.

Sandiford, M., Fraser, G., Arnold, J., Foden, J., Farrow, T., 1995. Some causes and consequences of high-temperature, low-pressure metamorphism in the eastern Mt Lofty Ranges, South Australia. Aust. J. Earth Sci. 42, 233–240.

Sandiford, M., Hand, M., McLaren, S., 1998a. High geothermal gradient metamorphism during thermal subsidence. Earth Planet. Sci. Lett. 163, 149–165.

Sandiford, M., Paul, E., Flottmann, T., 1998b. Sedimentary thickness variations and deformation intensity during basin inversion in the Flinders Ranges, South Australia. J. Struct. Geol. 20, 1721–1731.

Scherer, E.E., Cameron, K.L., Blichert-Toft, J., 2000. Lu–hf garnet geochronology: closure temperature relative to the Sm–Nd system and the effects of trace mineral inclusions. Geochim. Cosmochim. Acta 64, 3413–3432.

Seydoux-Guillaume, A.-M., Paquette, J.-L., Wiedenbeck, M., Montel, J.-M., Heinrich, W., 2002. Experimental resetting of the U–Th–Pb systems in monazite. Chem. Geol. 191, 165–181.

Skora, S., Baumgartner, L.P., Mahlen, N.J., Johnson, C.M., Pilet, S., Hellebrand, E., 2006. Diffusion-limited REE uptake by eclogite garnets and its consequences for Lu–Hf and Sm–Nd geochronology. Contrib. Mineral. Petrol. 152, 703–720.

Stacey, J.S., Kramers, J.D., 1975. Approximation of terrestrial lead isotope evolution by a two-stage model. Earth Planet. Sci. Lett. 26, 207–221.

Suzuki, K., Kato, T., 2008. CHIME dating of monazite, xenotime, zircon and polycrase: Protocol, pitfalls and chemical criterion of possibly discordant age data. Gondwana Res. 14, 569–586.

Taylor, S.R., McLennan, S.M., 1985. The Continental Crust: Its Composition and Evolution. Blackwell Scientific.

Thirlwall, M.F., Anczkiewicz, R., 2004. Multidynamic isotope ratio analysis using MC–ICP–MS and the causes of secular drift in Hf, Nd and Pb isotope ratios. Int. J. Mass Spectrom. 235, 59–81.

Vermeesch, P., 2018. IsoplotR: a free and open toolbox for geochronology. Geosci. Front. 9, 1479–1493.

Wade, C.E., 2011. Definition of the mesoproterozoic ninnerie supersuite, Curnamona Province, South Australia. Mesa J. 62, 25–42.

Webb, G., Crooks, A.F., 2003. A metamorphic investigation of the Palaeoproterozoic metasediments of the Willyama Inliers, southern Curnamona Province, South Australia. Results from literature review, fieldwork, petrography, and the spatial distribution of metamorphic minerals. In: South Australia Department of Primary Industries and Resources Report Book, 11.

Whitney, D.L., Evans, B.W., 2010. Abbreviations for names of rock-forming minerals. Am. Mineral. 95, 185–187.

Williams, M.L., Jercinovic, M.J., Harlov, D.E., Budzyń, B., Hetherington, C.J., 2011. Resetting monazite ages during fluid-related alteration. Chem. Geol. 283, 218–225.